HUNTING FOR MHZ GRAVITATIONAL WAVES WITH THE FERMILAB HOLOMETER

By

Brittany Lehua Kamai

Dissertation

Submitted to the Faculty of the
Graduate School of Vanderbilt University
in partial fulfillment of the requirements
for the degree of
DOCTOR OF PHILOSOPHY
in
Physics

August, 2016

Nashville, Tennessee

Approved:

Andreas A. Berlind, Ph.D.

J. Kelly Holley-Bockelmann, Ph.D.

M. Shane Hutson, Ph.D.

Stephan S. Meyer, Ph.D.

Keivan G. Stassun, Ph.D.

PHYSICS

HUNTING FOR MHZ GRAVITATIONAL WAVES WITH THE FERMILAB HOLOMETER

BRITTANY LEHUA KAMAI

Dissertation under the direction of Andreas A. Berlind, Ph.D.

A new ground-based detector, the Fermilab Holometer, has extended the accessible gravitational wave frequency range from kHz up to MHz. At these higher frequencies, exotic sources that were produced shortly after the Big Bang could radiate. The existence of nearby remnants is tested using the Holometer, which consists of separate yet identical 39-meter Michelson interferometers operated at Fermi National Accelerator Laboratory. Utilizing a 130-hour dataset collected between July 15, 2015 and August 15, 2015, constraints are made on both the stochastic gravitational wave background and primordial black hole binaries.

The first result is a 3σ upper limit of the stochastic gravitational wave background at MHz frequencies. This is the only direct gravitational wave measurement at these frequencies. The Holometer 3σ upper limit on the energy density, Ω_{GW}, is 5.6×10^{12} at 1 MHz and goes up to 8.4×10^{15} at 13 MHz. This result is much higher than existing indirect measurements. However, this does place constraints on early universe models that predict large bursts of gravitational radiation in a narrow MHz band.

The second result is a measurement of in-spiraling primordial black hole binaries from 1 to 1.92 MHz. We report that there are no detectable primordial black hole binaries in the mass range $0.7 - 3.5 \times 10^{21}$ g between the earth and the moon. Utilizing the same dataset, an alternative analysis path can constrain primordial black hole binaries in the mass range from 0.6 to 2.5×10^{25} g which would increase the distance out to Jupiter. Additionally, the sensitivity of the Holometer with a new data acquisition system can constrain merging black hole binary pairs up to $\sim 10^{30}$ g within the Milky Way halo. This instrument opens up a new opportunity to improve measurements on one of the least constrained mass ranges for primordial black holes.

DEDICATIONS

To curiosity.

ACKNOWLEDGEMENTS

I would not be where I am today without the immense amount of support that I have received over the years. The famous Nigerian proverb of “It takes a whole village to raise a child” is very applicable to me. I can only scratch the surface here of the impact you all have had in my life.

I would like to thank the National Science Foundation for all of their financial support through every program I have been through from undergraduate all the way through graduate school. Thank you to the Universities Research Association for funding my research at Fermilab. Also, thank you to the Ford Foundation for the support in my final year.

I’d like to thank my academic homes that have given me incredible platforms to become deeply immersed in cutting edge science. To the Fisk-Vanderbilt bridge family for launching me into the science world, the Vanderbilt Physics & Astronomy department for supporting me and pushing me further with my research, to the Kavli Institute of Cosmological Physics for taking me in as one of their own and exposing me to incredible science, to the Fermi National Accelerator Laboratory for introducing me to the unique world of experimental physics at a national laboratory.

My Holometer team (Aaron Chou, Dick Gustafson, Craig Hogan, Ohkyung Kwon,

Bobby Lanza, Lee McCuller, Steve Meyer, Jon Richardson, Chris Stoughton, Ray Tomlin, Jim Volk, Sam Waldman, Rai Weiss), you are an impressive group of individuals of whom I have had the honor of working with. You challenged me to learn a huge array of physics from the nuts and bolts to the intricacies of developing and testing novel ideas in physics. All the while throwing in as many jokes as we could think up.

Chris Stoughton, I know I can always count on you for a laugh. Thank you for reminding me that “Everything is Awesome” and always looking out for me.

Aaron Chou, I enjoy how you always make time to have a conversation about anything from an intricate physics idea to fun places to travel.

Dick Gufstanson and Ray Tomlin, I appreciate all your patience with teaching me the ropes of becoming an experimentalist and the secret handshakes at Fermilab.

Rai Weiss, you have continuously been a source of inspiration. Not only are you a truly talented scientist, you treat everyone as equals regardless of where they came from or how much schooling they have had.

Lee McCuller, Bobby Lanza and Jonathan Richardson for all the stories we will share about the good ’ol days of grad school of moving this experiment from the beginning to the end. I have great memories of the late nights, bike rides through Fermilab and talking about how much we loved what we were doing.

Craig Hogan, as the Zenmaster of Physics, you have taught me so much about the craft of a scientist. I cherish our car rides out to Fermilab where we would passionately discuss anything from Quantum physics to hiking the Pacific Crest Trail. Thank you for constantly reminding me that I am a valuable member of the team.

To my committee (Kelly Holley-Bockelmann, Keivan Stassun and Shane Hutson), you have played such an active role in my development. Your enthusiasm, encouragement and willingness to help in any way that you could made my graduate school experience so enriching.

To my surrogate advisors : Kartik Sheth, your years of guidance, support and reflection has helped me navigate through it. Shane Larson, your infectious enthusiasm for science has kept me smiling and looking forward to more.

I am so unbelievably lucky to have found not one but two incredible PhD advisors (Steve and Andreas). Both of you have been so instrumental in pushing me further and keeping me happy and sane. I can't thank you enough for all the years we have spent together and the memories of my time with you will be deeply cherished.

Steve Meyer, from day one you have been been such an incredible spirit. I remember our first day together when you said "the only difference between you and me is that I have more experience" and within 10 minutes we were both on our feet a the chalkboard working out how interferometers work. I truly appreciate how you would adapt to any advising style I needed. I am so lucky to have spent so much time with you. You have really taught me how to do great physics and have a blast doing it.

Andreas Berlind, you are someone who has always had my best interest in mind. I remember when I was deciding on PhD projects and I asked you what's in it for you if I went off to work on the Holometer, you said "I want you to be the best little scientist you can be." You have selflessly spent so many hours sticking to those words from the line-by-line editing of my writing, to helping me identify my intellectual hurdles and never letting me leave without making sure I really understood it. Your compassion for my well being has always shown through above and beyond everything else. You are a wonderful person and have a great sense of enjoying life and great music.

I have been so lucky to have such wonderful friends from all across the world.

To my beautiful friends from Hawaii (Tricia Higa, Luly Cheng, Asiana Ponciano, Bob Phu, Gavin Tanaka, Vincent Balao, Nolaniander, Hornandez, Sheldon Nakashima, Kramer Hatae, Jobi Ishii, Stacia Ahina, Fifi, Kelly Mason, Meike deNooy, Jelleke deNooy, Robert deNooy, Alan Bennington-Castro, Carena Church), mahalo nui loa for all of your love and encouragement through all the years. I can't wait to come back and hang out in the ocean and sunshine with you.

To all my peeps I met in Nashville (247, Daniel Limbrick, Melanie Duncan, Meagan Lang, Scott Nizgoda, Trey Mack, Fabienne Bastien, Felipe Colazo, Jen Piscionere, Manodeep Sinha, Matthew Richardson, Michele Chreshfield, Yonah EtShalom, Jedidah Isler), it was wonderful to have such a fun spirited group of friends to share in hana clubs at JJs, poke bowls at Ken's and breakfast club where I always burnt the toast.

To all my deeply passionate friends I met in Chicago (Alissa Bans, Freddy Martinez, Kartik Prahbu, Alex Sippel, Squid, EvanBarrEvanBarrEvanBarr, Jackie Valdez, Steve Lieto, Peter Pan, Jesse Rose Adams, Frank Schufford, Brian Kroll, Mason Donahue, Aneila Hogan, Kate Malecek, Zoehyr Doctor), you have all been a source of inspiration and we have made great memories in this crazy city through the warmth and the freezing cold.

Jon Ching, we have come such a long way since we started our friendship back when we were 11. From our water sports to art, science, relationships and travels, I have learned so much and it is wonderful to have you to reflect on where we have been and where we are going.

Robin Harney, you always brighten my day with your presence, your thoughtful messages and warm, infectious happiness. I am so fortunate to be able to call you any time day or night and you are there for me. You as my third sister and you mean so much to me.

Stacey Lawrence, just thinking about you and our memories instantly make me laugh. It was so comforting to have you as we walked along parallel academic paths to figure out what are we doing and where are we going. Napkin science has been a valuable part of my ability to communicate science and I know when we are ready we will be in our science bus.

Yilen Gomez-Maqueo Chew, your friendship means the world to me. There are so many hours that we have logged on Skype supporting one another through dj after dj during hana clubs. Bug, you held my hand every time I needed it and you are my unfeeling brain that helps me process it all. I know that I would not be here without you and I am overjoyed that we are buddies.

Jen Helsby, I love how we amplify each other in to having amazing experiences. From dying our hair blue to being by my side when I needed someone the most. You are an incredible friend and I am so happy and proud of all that you do.

Doug Watson, you have taught me a lot in your wise old man ways from research to friendships. It was a blast transitioning from Nashville to Chicago with you.

Ellie Terrell, your infectious giggles and carefree approach to life is what makes being around you so special. I loved sharing in our cross-country moments and will never look at another Kum-n-Go the same again.

Joseph Bennington-Castro, I am so happy to have started physics with you and to enter this new world with a familiar face. I love what an amazing friend you are and am so impressed with the road you have taken.

Brent Brent Koehn, I am so unbelievably lucky to have started this amazing partnership with you. You are the kind of man girls dream of. You have been such an amazing addition to my life and I am so happy to have found you. I love being able to share with you all that I do and your hugs are always exactly what I need. Thank you for your whole-hearted support, understanding and feeding me pineapples.

To my family, I can not thank you enough for the unconditional love you have provided throughout my life.

Grami, you are one of the sweetest people who has ever lived. You are such a strong individual who is the brightest light in the room. I am so happy to have had the time with you that I did because you really did teach me to get outside and soak up as much life as I could.

Rachel and Carolyn Kamai, for being the best little gremlin sisters anyone could ask for. You both have had more of an influence on me than you will ever realize. Without you two, I may never have jumped into these grand adventures. Thank you so much for your love and excitement.

Dad, you have been an incredibly positive influence in my life. You showed your love so deeply for me in not only your words but your actions. Your constant development of analogies has deeply shaped the way I do and communicate science. I appreciate what a truly caring person you are and listening to your music brings me back to the comfort of being home.

Mom, you have no idea how much your spirit lives within me even while I am away from home. You have had a huge influence in how curious I am, especially the way I pay attention to the world. Thank you so much for being an extraordinary mom, friend and cheerleader. Your support has kept the wind in my sails when I thought my ship had sunk.

To anyone that I have missed writing your name down on this piece of paper, it does not mean that you have not been important to me. You have definitely given me the inspiration or motivation I needed at exactly the time I needed it.

To my village, mahalo nui loa a me aloha nui loa.

TABLE OF CONTENTS

Page

CHAPTER

LIST OF FIGURES

CHAPTER I

INTRODUCTION

I.1 Gravitational Waves

In 1915, Einstein developed a new theory of gravitation called General Relativity.[1;2] This description of gravitational interactions relates the energy-momentum of an object with the curvature of space-time. More massive objects curve space-time more strongly than less massive objects. A few predicted observables from General Relativity that are different from the Newtonian description of gravitational interactions include the precession of Mercury, gravitational lensing and the gravitational redshift of light. Each of these predictions along with many others have been rigorously verified over the past 100 years.

After his series of papers on General Relativity, Einstein proposed a unique new observable - gravitational waves - oscillations in the space-time metric that result in the stretching and squeezing of space and time itself[3]. As a gravitational wave passes, the distance between objects and the duration between events will become longer and shorter. These oscillations carry away energy in a new form of radiation, namely gravitational radiation, and are directly related to an object's energy-momentum and quadrupole moment.

Gravitational waves are an entirely new way of exploring the universe. Before September 2015, the way we understood the universe was solely through electro-magnetic radiation, cosmic rays and neutrinos. After September 2015, the first direct detection of gravitational waves from an orbiting system of two ~ 30 $M_\odot$ black holes was made with a new class of observatories.[4] This single observation, has provided us with entirely new insights into astrophysics[5] and fundamental tests of gravitation and space-time.[6] Gravitational waves will play a vital role in facilitating tests of physics, astrophysics and cosmology in the years to come.

I.2 Gravitational Wave Spectrum

Gravitational waves can come in a broad range of predicted frequencies. Figure 1 encapsulates what may be accessible in our universe through the active experiments designed to search for objects at many different frequencies.

In the frequency range from 10^{-16} to 10^{-15} Hz, experiments such as BICEP, KECK, SPT-3G and CMB-S4 will accurately map out the cosmic microwaves background polarization in multiple wavelengths and angular resolution. The goal is to measure imprints of gravitational waves on the polarization of light in the early universe from processes such as inflation or new models of physics. In the frequency range from 10^{-9} to 10^{-7} Hz, experiments such as PPTA[7], EPTA[8;9], NanoGrav[10] utilize radio wave measurements of an array of pulsars as a long baseline gravitational detector. The stability of the pulses are used to search for time delays induced from a gravitational wave source. At these frequencies, the likely sources are mergers of supermassive black holes which will provide unique insights into galaxy formation. In the frequency range from 10^{-4} to 10^{-2} Hz, a space-based gravitational detector, eLISA, is actively being developed.[11] This experiment will utilize a 10^6 km baseline interferometer to search for supermassive black holes in distant galaxies and will be sensitive enough to measure lighter mass objects in the Milky Way. In the 10 to 10^4 Hz range, ground based gravitational wave detectors such as the Laser Interferometeric Gravitational Wave Observatory (LIGO)[12;13;14], VIRGO[15;16] and GEO-600[17] have led the field to the direct detection of two merging stellar mass black holes. These experiments utilize km scale interferometers located at multiple sites around the earth. Predictions of merging events in the late stages of binary stellar remnants such as black holes and neutrons stars are predicted in this frequency range.

In the 10^6 - 10^7 Hz frequency range, the Holometer is a new ground-based gravitational wave detector. This experiment consists of a pair of co-located 39 meter interferometers optimally sensitive across a broadband range of MHz frequencies. The only other experiment performed at these frequencies was in a very narrowband using superconducting microwave cavities[18] This instrument is much smaller than the kilometer scale interferometers; however, it opens up the opportunity to hunt for sources in an entirely new frequency range.

I.3 MHz Sources from the Early Universe

Potential sources that could emit gravitational waves at MHz frequencies would have originated in the very early universe. During this era, the universe was undergoing extreme conditions that could have produced a variety of exotic phenomena. A brief summary of the current cosmological model informed from many different astrophysical observations followed by a discussion about what early universe models could be probed with a MHz gravitational wave detector will be described below.

I.3.1 Current Cosmological Model

The universe began in a hot, dense Big Bang followed by a period of inflation that rapidly stretched the universe out to a flat universe with small inhomogeneities in the energy-density field. The universe continued to expand and went through various phase transitions where the fundamental forces (strong, weak and electro-magnetic) decoupled from one another. A few seconds later protons and neutrons formed then a few minutes later the universe cooled enough for the formation of light particles (such as ^{1}H,^{2}H, ^{3}H, ^{3}He, ^{4}He, ^{7}Li) to occur. As the expansion continued, the dominant form of energy transitioned from radiation into matter. When the universe became transparent enough due to the formation of neutral atoms, 400,000 years after the Big Bang, light was able to free stream and this is the cosmic microwave background we measure today. As the expansion continued, the formation of the first stars and galaxies began and continued to form further generations of stars and galaxies. Today, 14 billion years later, the large scale structure of the universe, from clusters of galaxies to filaments and voids, are a direct result of the inhomogeneities of the early universe.

This picture still has quite a few mysteries and a complimentary probe of gravitational waves can provide new insights to the electro-magnetic observations. One of the mysteries of the early universe is that of the period of rapid inflation that likely occurred at 10^{-35} seconds after the Big Bang.[19] It is unclear why this happened or what drove this phenomenon. Rich theoretical investigations provide models such as slow roll inflation[20;21], axion inflation[22] and a number of other inflationary models that predict what the fluctuations in the density field may be. The gravitational interactions with the density fields themselves could produce an observable gravitational radiation background.[23] Another inflationary observable could come from the formation of primordial black holes in over dense regions.[24;25] The range of primordial black hole masses could be as small as 10^{-5} g to as large as 10^{38}g(10^{5} $M_\odot$).[25] Masses smaller than 10^{15}g would have evaporated in the early universe due to Hawking radiation and left imprints on the CMB anisotropies and polarization.[26] Primordial black holes $> 10^{15}$g could still be around today and will be discussed further below.

Another set of early universe mysteries come from phase transitions such as the electro-weak decoupling at 10^{-11} seconds after the Big Bang along with the quark-hadron transition at 10^{-6} seconds. Possible consequences include the production of topological defects in space-time such as branes, cosmic (super-)strings and monopoles. Networks of these topological defects would also produce fluctuations in the density field in a uniquely different way than those predicted from the inflationary models. Cosmic string networks have been proposed to produce unresolved background gravitational radiation.[27] Individual cosmic strings would be an additional early universe relic[28;29;30] Another gravitational wave observable would be the collision of vacuum bubbles that formed from either phase transitions or inflation.[31] This would result in a peak in the predicted spectrum of an unresolved gravitational wave background or a large flux of gravitational radiation in a narrow frequency range.

This thesis will focus on placing constraints on the unresolved gravitational wave background along with a search for primordial black holes.

I.3.2 Unresolved Gravitational Wave Background

A superposition of a many gravitational wave sources would produce an unresolved gravitational wave background. One way to parameterize this background is called the Stochastic Gravitational Wave background (SGWB).[32] SGWB can be described through its contribution to the energy density Ω_{GW} which is the ratio of the energy density in the form of gravitational waves to the critical density of the universe, ρ_c.[32] The early universe processes described above make predictions for the amount and spectral shape of energy density, which scales roughly as f^{-3} , where f is the frequency.

Constraints on the abundance from stochastic gravitational wave backgrounds come from different probes as summarized in Figure 2. There are two classes of constraints which are indirect (CMB, BBN and LSS) and direct (Pulsar timing arrays, LIGO/VIRGO) gravitational wave probes. The indirect constraints place limits based on the amount of energy injected into the early universe that could be still be consistent with the measured observables. For instance, if there were too many primordial black holes, that would change the predicted chemical abundances making them inconsistent with measurements.[33] Similar arguments about processes that would introduce additional forms of energy would alter the measured anisotropies of the CMB power spectrum along with inducing spectral distortions to the near perfect blackbody measurements from FIRAS (a CMB experiment onboard the COBE satellite)[34;35]. Therefore, the BBN and CMB measurements are integrated constraints across many decades of gravitational wave frequencies.

Direct constraints come from gravitational wave experiments such as pulsar timing arrays, bar detectors, microwave cavities and ground based interferometers. Pulsar timing arrays place a constraint in the band 10^-9 Hz frequency range. In the 100Hz to 1kHz frequency range, the most sensitive measurement on the SGWB limit is set from the interferometer measurements from LIGO and Virgo rather than the previous constraints from bar detectors and microwave cavities.[32;37;38;36] The interferometer measurement of the SGWB cross-correlates the output of multiple interferometers such as the combination of LIGO-Livingston, LIGO-Hanford and Virgo. Another set of measurements was from two of the LIGO detectors which were co-located at Hanford washington. This combination of detectors gives an improved constraint because there is a lack of signal decoherence over the larger baseline from the global network of detectors. To date, there are no direct measurements in the MHz band which the Holometer is uniquely sensitive to.

I.3.3 Resolvable Remnants : Low Mass Primordial Black Holes

Primordial black holes form in the early universe where inhomogeneities in the energy density field can compress into black holes. The mass of the black holes depend on the epoch that the black holes are formed as defined by

$$\mathrm{M_{PBH}} = \frac{\mathrm{c^3 t}}{\mathrm{G_N}} \tag{1}$$

where $\mathrm{M}_{\mathrm{PBH}}$ is the mass of the primordial black holes, c is the speed of light, t is the formation time after the big bang, G_{N} is the Newtonian gravitational constant.[25] Black holes formed in the early universe will typically stay the same size as they were at the time of formation.[25] Black holes smaller than 10^{33} g(1 $\mathrm{M}_{\odot}$) could only have formed in the early universe because astrophysical processes could not compress anything smaller.[39]

The primordial black holes that mainly considered are ones formed during the radiation dominated period that took place after inflation, which was from 10^{-35} seconds to 5,000 years after the Big Bang. Primordial black holes formed before inflation will have a number density that is much less than the ones formed later. The fraction of primordial black holes, $\beta(M_{\mathrm{PBH}})$ that would still be around today (14 million years after the Big Bang) is given by the following equation :

$$\beta(M_{\mathrm{PBH}}) = 1.15{\times}10^{-18}\gamma^{-1/2}\left(\frac{\gamma\, M_{\mathrm{PBH}}\, n_{\mathrm{PBH}}(t_0)}{\rho_c}\right)\left(\frac{h}{0.72}\right)^2\left(\frac{g_{*i}}{106.75}\right)^{1/4}\left(\frac{\gamma\, M_{\mathrm{PBH}}}{10^{15}[\mathrm{g}]}\right)^{1/2} \tag{2}$$

where γ a numerical factor that depends on the details of gravitational collapse and can range from as small as 10^{-4} to $>> 1$, $\mathrm{M}_{\mathrm{PBH}}$ is the mass of the primordial black holes, $n_{\mathrm{PBH}}(t_0)$ is the number of primordial black holes today (t_0), ρ_c is the critical density required to make a spatially flat universe, h is the Hubble parameter which is the expansion rate of the universe normalized by 100 [km/s/Mpc], g_{*i} counts the relativist degrees of freedom which is normalized to the value of g_* at 10^{-5} s, an epoch where most of the primordial black holes are likely to have formed and $[g]$ is the unit grams.[26]

Primordial black hole constraints are based on many different astrophysical probes as seen in Figure 3. For convenience, the mass fraction of primordial black holes is redefined as[26]

$$\beta'(M) \equiv \gamma^{1/2} {\frac{g_{*i}}{106.75}}^{-1/4} \beta(M) \tag{3}$$

Masses $< 10^{15}$ g would have evaporated in the early universe due to Hawking radiation, masses $\sim 10^{15}$ g would be evaporating today and masses $> 10^{15}$ g would still be around today. Masses from 0 to 10^4 g are constrained by the Planck mass relics' contribution to the dark matter fraction (Planck). Masses from 10^4 to 10^8 g are constrained by evaporating primordial black holes into LSP (the lightest supersymmetric particle). Alternatively, if inflation did not happen than limits can be placed by the primordial black hole contributions to the entropy of the universe. Masses from 10^8 to 10^{14} g are constrained by their effects on Big Bang nucleosynthesis (BBN) and the cosmic microwave background (CMB). If there were too many evaporating primordial black holes than it would effect the measured abundances of light nuclei and the fluctuations in the CMB power spectrum. Masses from 10^{14} to 10^{18} g are constrained from measurements of the extra galactic background (EGB) and galactic gamma ray background (Galactic γ). These constraints are based on the amount of emission that would be created through accretion onto the primordial black holes. The dashed lines in this mass range correspond to the improvements from using 21 cm intensity mapping of the matter field. Masses from 10^{18} to 10^{22} g are constrained from are from femto- and pico- lensing of gamma ray bursts. Masses from 10^{22} to 10^{28} g are constrained through a density limit of the smallest unevaporated black holes, $\Omega_{\rm PBH}$, that is consistent with the Galactic γ ray limit. Masses from 10^{28} to 10^{33} g are constrained from FIRAS measurements of spectral distortions of the CMB. If the black holes were accreting in the early universe, the increased photon emission would add extra energy into the radiation field that would effected the perfect blackbody of the CMB. Masses from 10^{33} to 10^{35} g are constrained from lensing of distant quasars (QSO). Masses from 10^{35} to 10^{38} g is constrained from disruption of wide stellar binary systems (WB). In this mass range, there are strong constraints from the direct emission of gravitational wave for masses between 10^{36} to 10^{37} g (GW). The MACHO experiment which uses micro-lensing of stars places additional constraints on masses from 10^{32} to 10^{40} g. Masses from 10^{38} to 10^{46} g are constrained by the large-scale structure of galaxies (LSS) and dynamical friction (DF). Large primordial black holes would have altered the initial matter field of the universe and changed the structure of galaxies we see today. The dynamical friction constraints are from the effects primordial black holes would have on the formation of individual galaxies and clusters. Masses from 10^{46} to 10^{50} g are also constrained density limits from the gamma ray background. The measurements from the CMB temperature anisotropies help to constrain the mass range from 10^{33} to 10^{49}.

The least constrained regions are the range from $10^{20} - 10^{26}$ g and $10^{2} - 10^{4}$ $M_{\odot}$.[26] The Holometer provides a unique new probe in the mass range from 10^{21} to 10^{30} g region which will be discussed further Section IV.1.2.

I.3.4 Additional Exotic Sources

As mentioned earlier, there could be additional remnants that the Holometer is sensitive to such as cosmic super-strings and bubble collisions. Cosmic super-strings oscillate at the speed of light and emit gravitational radiation during these oscillations. Additionally, a kink or break in a cosmic super-strings breaks can produce gravitational radiation. Therefore, it is possible to search for either stable or bursting cosmic super-strings with a gravitational wave detector.[30] Additionally, bubble collisions from phase transitions could also produce a large spike in a narrow-band of frequencies. These searches are capable with this dataset.

The focus of this thesis will be using the Holometer to place constraints on the Stochastic Gravitational Wave Background and the Primordial black holes at MHz frequencies.

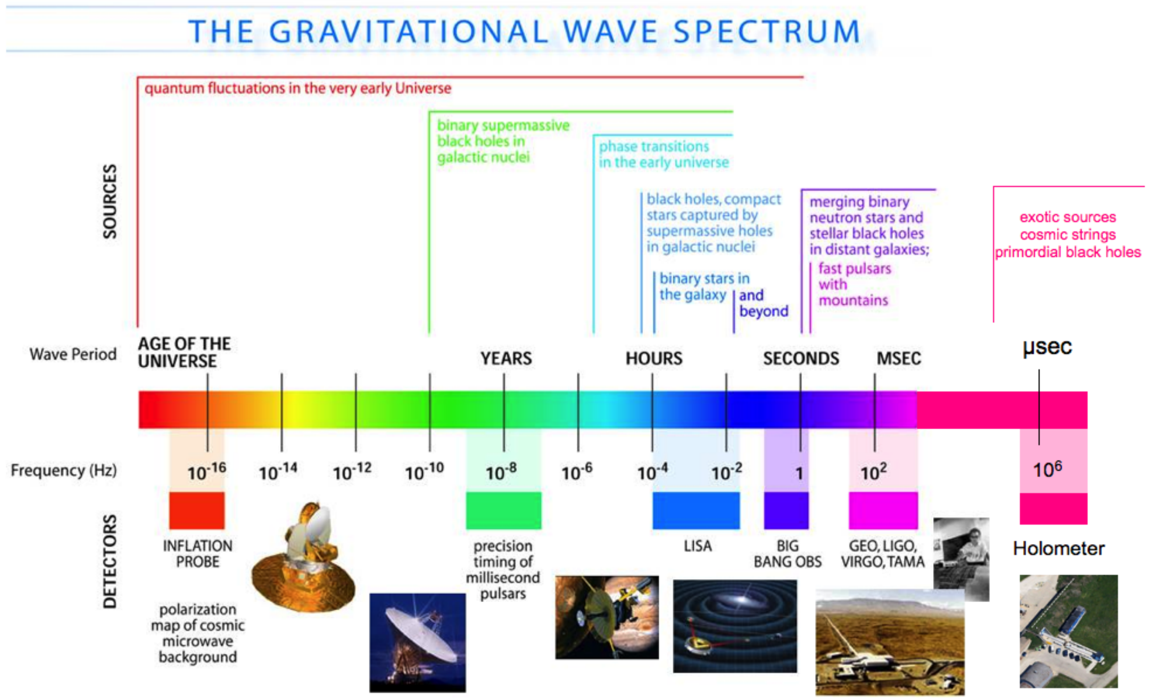

Figure 1 The gravitational wave spectrum spanning from the lowest to the highest frequencies. This spectrum encapsulates the type of sources that would be accessible in each frequency range and the experiments that are designed to detect them. In the frequency range from 10^{-16} to 10^{-15} Hz, gravitational wave signatures will be imprinted on the polarization of the cosmic microwave background from physics in the early universe. In the frequency range from 10^{-9} to 10^{-7} Hz, pulsar timing arrays are employed as a long baseline gravitational detector in the search for merging binary supermassive black holes. In the frequency range from 10^{-4} to 10^{-2} Hz, a million kilometer space-based interferometer will be used to search for supermassive black holes capturing stellar remnants along with lighter mass stellar remnant pairs like neutron stars in the Milky Way galaxy. In the 10 to 10^3 Hz range, kilometer scale gravitational wave detectors on earth are designed to measure the last phase of merging events from stellar remnants such as black holes and neutron stars. In the 10^6 to 10^7 Hz range, ground-based decameter scale gravitational wave detectors may be sensitive to early universe remnants such as primordial black holes and cosmic (super-)strings.

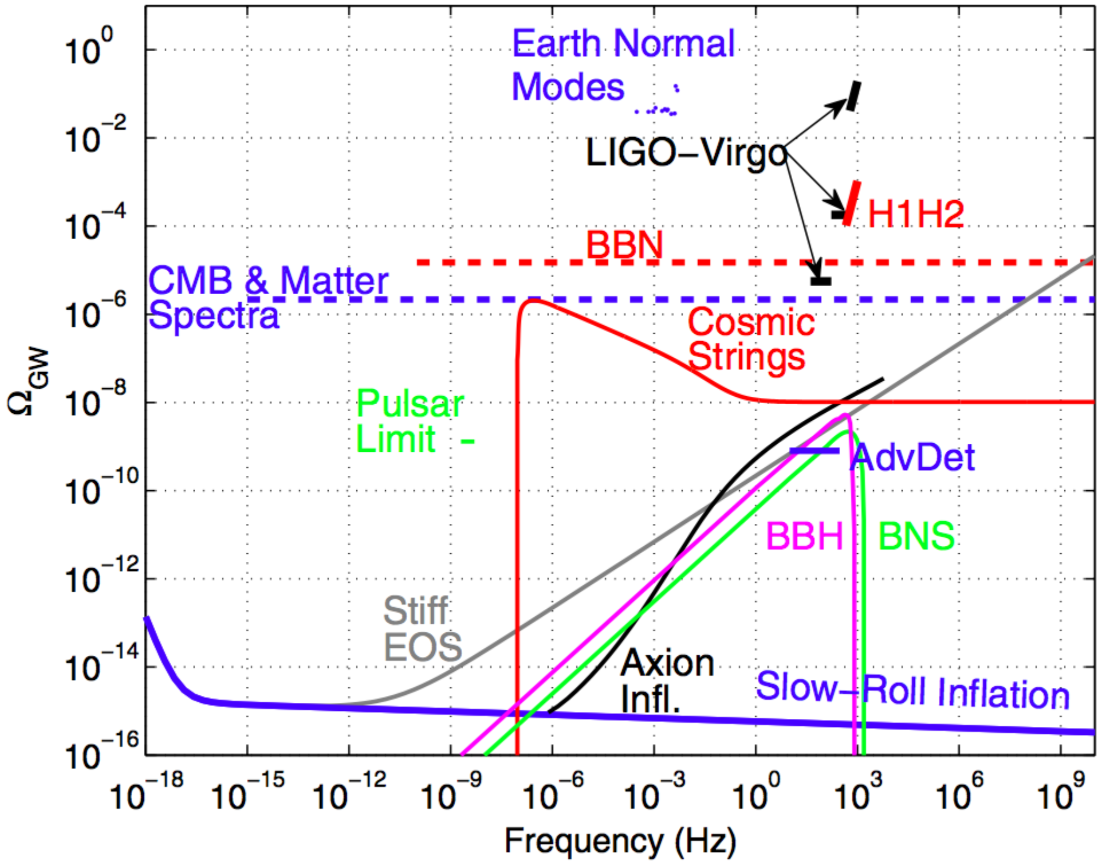

Figure 2 Constraints on the energy density of stochastic gravitational waves, Ω_{GW}, as a function of frequency[36] This figure describes the landscape of both experimental constraints and theoretical predictions. The indirect experimental constraints are from Big Bang Nucleosynthesis (BBN), Cosmic Microwave Background (CMB) and Matter power spectra. These measurements constraint the abundance of gravitational waves by their effects on the production of light nuclei in the early universe, the anisotropies and spectral distortions of the radiation in the early universe and the late time structure growth. The direct experimental constraints are from Pulsar timing arrays, Earth Normal modes, LIGO-Virgo, and LIGO H1 - LIGO H2 (where H1 and H2 indicate two co-located interferometers at the Hanford, Washington site). Each of these measurements place upper limits on the abundance of the stochastic gravitational wave background contributing to the overall noise budget. The line for advanced-LIGO (AdvDet) shows the projected constraints with new upgrades to the detectors. Additionally, this figure shows the predicted spectral shape for a few early universe models such as slow-roll inflation, axion inflation[22], stiff equation of state and cosmic strings. The other curves (BBH and BNS) are predicted contributions at late time populations of binary black holes and binary neutron stars. Current predictions from these late-time populations will not have any signal up at MHz frequencies. The Holometer will be the first experiment to place constraints in the MHz frequency range.

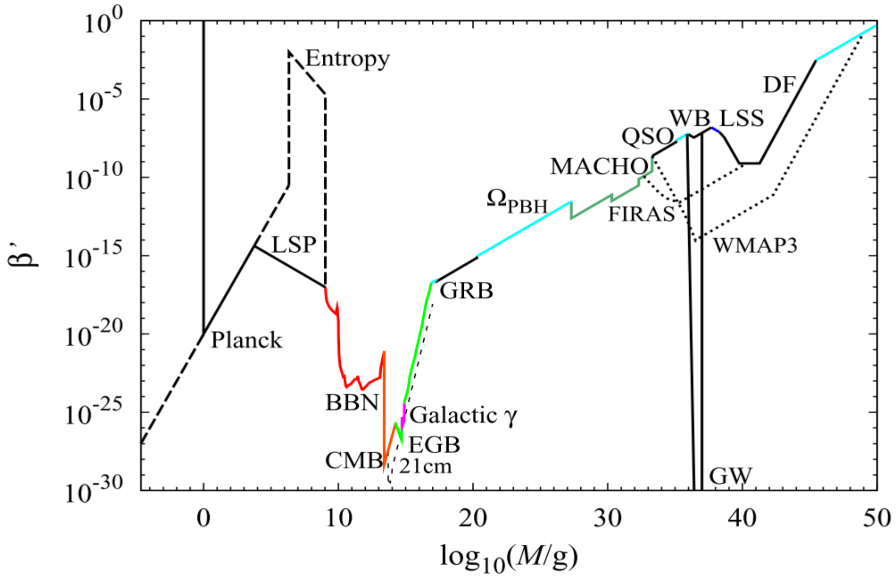

Figure 3 Constraints on the fraction of primordial black holes, β', as a function of mass, which are defined in Equations 1 and 3.[26]. Masses from 0 to 10^4 g are constrained by the Planck mass relics' contribution to the dark matter fraction (Planck). Masses from 10^4 to 10^8 g are constrained by evaporating primordial black holes into LSP (lightest supersymmetric particle). Alternatively, limits can be placed by the primordial black hole contributions to the entropy of the universe (Entropy). Masses from 10^8 to 10^{14} g are constrained by their effects on Big Bang nucleosynthesis (BBN) and the cosmic microwave background (CMB). Masses from 10^{14} to 10^{18} g are constrained by measurements of the extra galactic background (EGB) and galactic gamma ray background (Galactic γ). Additional improvements in this range will be made with future 21cm measurements (dashed line). Masses from 10^{18} to 10^{22} g constraints are from femto- and pico- lensing of gamma ray bursts. Masses from 10^{22} to 10^{28} g are constrained through a density limit of the smallest unevaporated black hole, Ω_{PBH}, that is consistent with the Galactic γ ray limit. Masses from 10^{28} to 10^{33} g are constrained from FIRAS measurements. Masses from 10^{33} to 10^{35} g are constrained from lensing of distant quasars (QSO). Masses from 10^{35} to 10^{38} g are constrained from disruption of wide stellar binary systems (WB). In this mass range, there are strong constraints from the direct emission of gravitational waves for masses between 10^{36} to 10^{37} g (GW). The MACHO experiment which uses micro-lensing of stars places additional constraints on masses from 10^{32} to 10^{40} g. Masses from 10^{38} to 10^{46} g are constrained by the large-scale structure of galaxies (LSS) and dynamical friction (DF). Large primordial black holes would have altered the initial matter field of the universe and changed the structure of galaxies that we see today. The dynamical friction constraints are from the effects primordial black holes would have on the formation of individual galaxies and clusters. Masses from 10^{46} to 10^{50} g are also constrained by density limits from the gamma ray background. The measurements from the CMB temperature anisotropies help to constrain the mass range from 10^{33} to 10^{49}. One of the least constrained regions is the range from $10^{20} - 10^{26}$ g and the Holometer provides a unique new probe within this mass range (SectionIV.1.2).

CHAPTER II

THE FERMILAB HOLOMETER

II.1 Ground-based Gravitational Wave Detectors

Gravitational waves are described by the frequency and amplitude of the oscillations. The frequency of the wave depends on its source as mentioned in Section I.2 and Section I.3. The amplitude of the gravitational wave is called the strain, which is the fractional change in the stretching and squeezing of the space-time metric. Sources such as stellar mass black hole binaries are predicted (and measured) to create fractional changes in the space-time metric by 10^{-22} at 100 Hz.

The detectability of a gravitational wave depends not only on the type of source but also on the distance to the source and the sensitivity of the instrument. The most sensitive ground based detectors are large scale Michelson Interferometers. Over the last ∼40 years, the LIGO collaboration has pioneered the technology to be able to make a detection from earth. LIGO/VIRGO/GEO-600/KAGRA are broadband detectors sensitive to gravitational waves across a range of frequencies from 10 Hz to 1kHz. Other types of ground-based detectors exist such as resonant bar detectors and superconducting microwave cavities though they are sensitive in a very narrow range of frequencies.

A Michelson interferometer is an instrument that converts the gravitational wave strain into a measurable effect via changes in the distance light travels in two orthogonal paths. As a gravitational wave passes through a Michelson interferometer, it increases the physical length of one arm while shrinking the length of the other. This lengthening and shrinking is directly proportional to the frequency of the gravitational waves. The technological feat that the kilometer scale interferometers needed to achieve was to suppress physical length changes due other effects such as seismic variations, Newtonian gravitational gradients which are over 10 orders of magnitude at some frequencies[13]. Additional challenges to overcome in this measurement were effects to the optics from thermal coating noise and lensing effects and even the limitations imposed on the measurement from standard quantum mechanics. To verify that the measured length changes are real effects from gravitational wave emitting sources, multiple kilometer scale interferometers were built around the world.

The Holometer is a new broadband detector that is sensitive to gravitational waves at much higher frequencies (MHz). This instrument is a smaller, simpler pair of large scale Michelson interferometers. One advantage this instrument has over the others is that by operating at MHz frequencies the dominant noise source is photon shot noise rather than the seismic, optical and quantum noise the others need to suppress. Details of the Holometer design and performance will be described below.

II.2 Anatomy of the Fermilab Holometer

The Holometer consists of a pair of 40 meter Michelson interferometers constructed and commissioned at Fermi National Laboratory between 2009-2014 as seen in Figure 4. Each interferometer has parallel but independent systems - equipped with separate lasers, housed in separate vacuum systems, operated with separate electrical systems, separate signal detectors and uses separate digitizers. The goal of this design is to reduce known correlations between the two interferometers. The laser wavelength used is 1064nm produced from an Nd:Yag crystal. The ultra-high vacuum systems for each interferometer are stably operated at 10^{-8} Torr . Each interferometer is a power-recycled Michelson interferometer that is capable of making instantaneous length measurements down to 10^{-18} m/$\sqrt{\text{Hz}}$, which will be described below in detail.

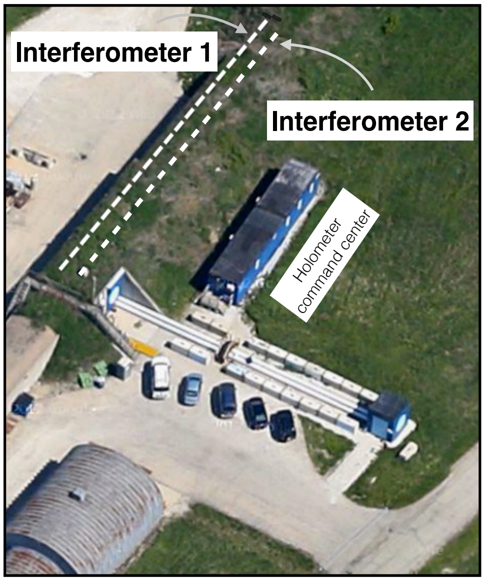

Figure 4 Google Earth image of the Holometer at Fermi National Accelerator Laboratory. The Holometer consists of two 39-meter Michelson Interferometers (pink arrow) separated by 0.6 meters. Both interferometers are completely isolated in separate vacuum systems. Half of each interferometer is inside a tunnel while the other half extends outside to a blue hut. The optical path of the interferometers will be described in Section II.3. The Holometer command center is where the computers that processes the data are.

II.3 Power-Recycled Michelson Interferometer

A simple Michelson interferometer uses 3 core optics - a beamsplitter and two distant end mirrors as seen in Figure 5. The laser injected into the interferometer interacts with the beamsplitter, an optic that is coated to be 50% transmitting and 50% reflecting. This incident beam samples the beamsplitter's position in two orthogonal directions and travels the length of the instrument. At 40 meters away, the distant end mirrors reflect 100% of the light back towards the beamsplitter. The interferometer is set up to have the returning beams recombine at the beamsplitter. After the beams recombine, any in-phase light returns towards the laser while any out-of-phase light exits the interferometer.

The instrument's sensitivity to gravitational waves depends on the amount of power in the Michelson interferometer. A technique used to increase the power is known as power-recycling, which increases the amount of photons on the beamsplitter. It combines a Michelson interferometer with a Fabry-Perot cavity to reuse photons that would otherwise return directly towards the incident laser. The advantages of power-recyling are an increase in the length sensitivity of the interferometer, laser frequency stabilization through the Pound-Drever-Hall technique[40] and as a filter from additional unwanted noise that would otherwise enter the interferometer.

II.4 Measurement of Interest : Differential Arm Length

The main measurement of a Michelson interferometer is any out-of-phase light from differential changes in the path length ($\Delta L = L_1 - L_2$), nominally referred to as DARM. Changes in the arm length produce a phase shift between the returning beams, which results in destructive interference from the light not perfectly canceling. This is measured in the detectors as power variations. The signal exiting the interferometer carries information about any longitudinal variation between the beamsplitter and the end mirrors.

By utilizing a high finesse Fabry-Perot cavity in the Holometer, we can reach $\sim$2.5 kW of circulating power within the interferometer from a 1 W incident laser. The increased power increases the number of photons sampling the length variations and reduces the shot noise by $1/\sqrt{\mathrm{N_{photons}}}$. Shot noise is calculated in the following way : $\Delta\,\mathrm{x_{shot}} = 1/2\pi\sqrt{\mathrm{h\,c}\,\lambda/\mathrm{P_{beamsplitter}}}$ where h is Planck's constant, c is the speed of light, λ is the wavelength of light (which is 1064 nm in this case) and $P_{\mathrm{beamsplitter}}$ is the amount of power on the beamsplitter. For 1 W of power on the beamsplitter, $\Delta\mathrm{x_{shot}} = 7.3 \times 10^{-17}\ \mathrm{m}/\sqrt{\mathrm{Hz}}$ whereas with 2.5 kW this improves by over an order of magnitude to $1.5 \times 10^{-18}\ \mathrm{m}/\sqrt{\mathrm{Hz}}$. At MHz frequencies, photon shot noise is the largest sources of noise.

II.5 Holometer Layout

Figure 6 shows a simplified layout of the Holometer optical system and highlights the channels that are digitized and used for scientific analysis. As mentioned in Section II.2, the interferometers are separate yet identical and kept isolated from one another until the final step of computation. Figure 6 has five main features to it :

1. Power Recycled Michelson Interferometers

    (a) There are two identical 39 meter Power-Recycled Michelson Interferometers.
    (b) Details of Power-Recycled Michelson Interferometers are described in Section II.3.
2. Interferometer signal detectors
    (a) The interferometer signal detectors measure the differential arm length measurement described in Section II.4.
    (b) Each interferometer is equipped with 2 separate signal detectors which will be described in Section II.6.
3. Environmental monitors
    (a) Environmental monitors are set up to measure any ambient noise that would enter into the system and produce correlated noise.
    (b) The are monitors are an antenna, laser phase monitor and laser amplitude monitor which will be described in Section II.10.
    (c) Details of how we use the monitors to reject contaminated frequency bins will be described in Section II.11.2.
4. Digitizers
    (a) There are four separate analog-to-digitial converters (ADCs) that sample and digitize the signal at 50 MHz.

   (b) Each digitizer has 2 channels that results in a total of 8 channels available for digitization.
   (c) The input signals are from the interferometer signal detectors, loop antenna, phase and amplitude monitors.
   (d) During science operations, the environmental monitors were rotated through because there are more monitors than available channels. A amount of live time during the run is also described in Section II.10.

5. Computer
   (a) The digitized signals are sent via a 40 meter fiber optic cable to the 32-core processor computer which processes the data.
   (b) Details of the data acquisition pipeline will be discussed in Section II.7.

II.6 Signal Detectors

At the output port of the power-recycled Michelson interferometer, the exiting beam is split off into two signal detectors. This output design of using two detectors is specific to the Holometer and is not a general necessity at the output of Michelson interferometers. Each signal detector is a NewFocus 1811 detector modified to be shot-noise limited at 10 mW (meaning the dominant noise source is the photon counting statistics and not the detector electronics) and can handle up to 150 mW of power. These detectors have both a DC output port, which has a voltage proportional to the average amount of intensity fluctuations, and an AC port that amplifies the intensity fluctuations about this mean value. The Holometer modification to the initial commercial circuit design used an inductor to shunt off most of the photocurrent into the DC channel. This allows for more incident power (150mW) while not saturating the amplifiers in the AC chain. The DC chain amplifies the detectors by a factor of 10 while the AC channel amplifies the signal by 10^4. The dark noise of the AC channel of a representative detector is shown in figure (dark noise picture). This modified NF1811 has a high pass filter that turns on at 500 kHz and loses response at 25 MHz. The AC channel is fed directly into the beginning of the data acquisition pipeline (DAQ).

II.7 Data Acquisition Pipeline

All the analysis for the Holometer must be performed in the frequency domain due to the high demands of the sampling rate, which differs drastically from other gravitational wave searches that perform searches by template matching in the time domain.

Figure 7 illustrates the main steps from sampling the time stream into the final hdf5 files. This figure simplifies the steps to only describing 2 channels while in reality there are a total of 8 channels where all these computations take place. In step 1, the voltage is sampled at 50 MHz resulting in a time stream instance, V_k, of 65,445 individual voltage measurements. Each subsequent time stream instance is stored in the buffer for a duration of 1 millisecond. After 1 millisecond, the Fourier transform is performed on the data to transform into the frequency domain

$$A(f)e^{i\theta(f)} = \sum_{k=1}^{130,890} e^{i\,2\pi\,f_j\,t_k}\,V_k \tag{4}$$

where V_k is the time stream instance in volts, f_j is the frequency in Hz and t_i is time in seconds. This Fourier transform is computed for each of the separate channels and will be referenced as $A_a(f)\,e^{i\theta_a(f)}$ and $A_b(f)\,e^{i\theta_b(f)}$ for channels a and b, respectively. Additionally in each millisecond, the spectral densities are computed as illustrated in step 2 of Figure 7. Generically, the cross-correlation C^{xy} between the Fourier transforms of some channel x, C^x, and the complex conjugate of some channel y, C^{y*} is computed as

$$C^{xy} = C^x C^{y*} = A_x A_y e^{i(\theta_x - \theta_y)} \tag{5}$$

C^{xy} is the power in V^2 and to convert it into spectral density units V^2/Hz by dividing by the frequency bin size, which is 382 Hz in our case. The power spectral density (PSD) is the case when $x = y$ and the cross spectral density (CSD) is when $x \neq y$. Therefore, the power spectral density of channel a is $C^{aa} = |A_a|^2$ and channel b is $C^{bb} = |A_b|^2$. The cross spectral density between channel a and b is $C^{ab} = A_a A_b e^{i(\theta_a - \theta_b)}$. For the individual channels, the power spectral density is a real-valued function which is a measurement of the amount of power in each frequency bin. Whereas the cross-spectral density is a complex function that is a measurement of the amount of correlated power in each frequency bin between the two channels.

Over the next 1 second, 1,400 millisecond PSDs and CSDs are averaged together as illustrated in step 3 of Figure 7. At the end of each 1 second, the data is stored in an `hdf5` file with GPS timestamps to nanosecond precision. Steps 1-3 are repeatedly performed throughout the entire integration. The final `hdf5` file contains the PSDs for each of the 8 channels along with all of the CSDs for every combination of the different channels. Additional information such as the sampling frequency, equivalent noise bandwidth (ENBW), number of frequency bins used, along with scaling information to convert from ADC bits to volts are contained in each file.

II.8 Calibration from Volts to Meters

The physical quantity of interest is the physical arm length changes of the interferometer (DARM), which are in units of meters, whereas the final output of the data acquisition system is in volts. The science band of interest is in the MHz frequency range which makes applying a direct voltage to meters calibration a challenge. We developed a calibration ladder from low to high frequencies to state what the length fluctuations at MHz frequencies are.

1. Drive in a known signal to the end mirrors [$\Delta V_{\mathrm{in}}/\Delta \mathrm{m}$]
    (a) The end mirrors of the interferometers are mounted to piezo-electric actuators.
    (b) Sending in a drive signal [V_{in}] to the actuators pushes the end mirror [m].
    (c) The end mirrors can be driven this way up to 1kHz frequency.
2. Interferometer Response [$\Delta \mathrm{m}/\Delta \mathrm{W}$]
    (a) Driving the end mirrors changes the differences in the arm lengths (DARM).

    (b) The interferometer converts the drive signal [m] into intensity fluctuations [W].
    (c) Michelson interferometers respond differently than Power-Recycled Michelsons.
    (d) Measurements of the drive signal are done in Michelson mode.
    (e) Measurements of the drive signal are done in Power-Recycling mode.
    (f) Models of Power-Recycled Michelson response are compared to the measurements.

3. Detector Response [$\Delta\mathrm{W}/\Delta\mathrm{V}_{\mathrm{out}}$]
    (a) The light exiting the interferometer [W] is measured on a photodetector [A].
    (b) The detector electronics converts the photocurrent [A] into voltage [V].
    (c) The output of the detector has two channels - low and high frequency.
    (d) Low Frequency
        i. The response of the low frequency channel is measured.
        ii. The low frequency response is up to $\sim$ 200 kHz.
        iii. The drive signal is measured in the low frequency channel.
    (e) High Frequency (Signal Channel)
        i. The science band of interest is measured at high frequencies.
        ii. Measurements of the high frequency response are made.

iii. The high frequency response turns on at ~ 200 kHz.

iv. Measurements of the low frequency to high frequency response are performed.

  - *A signal driving an LED across many different frequencies was how this measurement was performed (no interferometer).*

All of these steps were performed multiple times throughout the commissioning and operations stages of the Holometer. For more details about how each step was performed see Lanza[41] and McCuller[42] . The final calibrations for the interferometers are $2.27 \pm 0.18 \times 10^{-12}$ [V/m] for Interferometer-1 and $3.01 \pm 0.18 \times 10^{-12}$ [V/m] for Interferometer-2. The calibration is applied after data taking is completed.

II.9 Operation of the Interferometers in Science mode

The goal of this experiment is to achieve the highest sensitivity to MHz length fluctuations in the search for gravitational wave sources. Achieving this goal requires a trade-off between the amount of power the detectors can handle, additional optical noise from impurities on the optics along with the stability of the interferometer relative to the environmental conditions. Each interferometer is operated near the dark fringe, which is the condition where the differential arm lengths perfectly cancel. To receive power on the detectors, the interferometers are held at δL ~ 1 nm to better than 0.1 Å fluctuations about that point. Each interferometer's control system maintains these operating conditions by using signals from light leaking out of the interferometer at the end mirrors along with light that exits at the signal port. Environmental conditions such as seismic variations, and various types of local ground motion can introduce enough noise to derail the control system and lose the stable operating point of a 1 nm offset.

During engineering campaigns, operators had to simultaneously control both interferometer's manually. The duty cycle was quite low roughly 10% because it was hard to have both interferometers maintaining long stable locks. An automated system was developed for the Holometer to quickly bring the interferometer back to its operating condition. With the automated system's implementation, operation has gone from having stable operating conditions for only a few minutes to uninterrupted hour long stretches.

In the beginning of the campaign, the duty cycle was highest at $\sim$ 90% in the evenings (after 5pm CST until 6 am CST) and weekends. However, it would fall to $\sim$ 50% during the daytime due to Fermilab activities. Halfway throughout this campaign, improvements to the automated system improved daytime stability to $\sim$ 90%. There was typically one operator running both interferometers to see if the duty cycle fell below $\sim$ 20%. Their role would be to make fine tune the interferometer's cavity axis by adjusting the injection alignment. Additionally, they would run scripts that monitor the interferometer's operating conditions for use in determining the calibration. A change that significantly improved the duty cycle and allowed us to move to remote operations was placing the injection mirrors on piezo-electric actuated mounts. After these changes, operators rarely needed to access the laser lab and could operate both interferometers on remote computers. This improvement drastically increased the number of operators along with the amount of science data that can be taken. These developments to the control system allowed us to take data up to the hundred hours reported in this study.

II.10 Science Data and Environmental Monitors

The science data used in this study was taken from July - August 2015, where 130 hours of data was collected. This constitutes to greater that 10^8 individual spectral measurements. Interferometer-1 was operating at $\sim$ 2.3 kW of power with $\sim$ 220 mW of cavity power leaving the interferometer. At these operating conditions, the sensitivity of the Interferometer-1 was $1.8\ \times 10^{-18}\,\mathrm{m}/\sqrt{\mathrm{Hz}}$. Interferometer-2 was operating at $\sim$ 2.5 kW of cavity power with $\sim$ 220 mW of power leaving the interferometer. At these operating conditions, the sensitivity of the Interferometer-2 was $2.2\ \times 10^{-18}\,\mathrm{m}/\sqrt{\mathrm{Hz}}$. The difference in sensitivity from the standard shot noise calculation for this amount of power is due to additional optical noise from impurities on the optics. The amount of exiting power was chosen to have more signal power than optical noise.

The data acquisition system is equipped with 4 separate ADCs that result in a total of 8 available channels. The first crate has both of the photodiodes from a single interferometer and the second crate has the both of the photodiodes from the second interferometer. The third and fourth crates are the auxiliary channels which we use as environmental monitors. The additional channels allow us to put constraints on the ambient RF environment, the influence of laser amplitude noise and laser phase noise contributions to the output signal measured by the interferometers. The cross-correlation is performed across all combinations of the 8 channels.

To monitor the ambient RF environment, a loop antenna passively monitored the environment above the signal detectors. During commissioning, this antenna along with a few other probe antennas were used to identify electronics that produced large amounts of RF noise. Our primary way to reduce the coupling between the electronics culprits and the signal detectors was to wrap the signal cables around ferrite cores. This reduced the common mode coupling in the electrical lines. The condition for acceptable suppression was that this noise would not couple into the signal at a detectable level until $\sim$ 1000 hours of integration was reached. The location of the loop antenna during science data taking was optimized for the region that would be most susceptible to RF noise.

The laser sine wave can be characterized by both its amplitude and phase, $A\, sin\theta$. Each laser has both laser amplitude noise $A \pm \delta A$ and laser phase noise $\theta \pm \delta\theta$. These fluctuations arise from different processes in the lasing medium and the stability of the laser electronics to produce a coherent laser beam. Any amplitude or phase fluctuations that enter the 40 m Michelson interferometer will produce additional noise on the DARM signal at the output port. To monitor the laser amplitude noise, we shunt less than 1% of the input beam into a separate high frequency detector that monitors the intensity fluctuations. The output of this detector is fed directly into the data acquisition system as the laser amplitude monitor.

To monitor the laser phase noise, we use the output from the Pound-Drever-Hall

(PDH) frequency stabilization signal. PDH is designed to stabilize any laser wandering by comparing it to a reference cavity[43]. The Fabry-Perot cavity of the power-recycled Michelson interferometer is the reference cavity of which the laser frequency is stabilized to.[40]. As part of the control loop that implements this stabilization, the laser frequency is actively monitored. Laser frequency and laser phase is the same quantity, so we can use this signal as our laser phase monitor. We perform an ex-situ calibration (V/m) of the PDH phase noise signal using a small Mach-Zehnder interferometer on the laser table. The Mach-Zehnder interferometer works by splitting the light down two paths similar to a standard Michelson interferometer. The difference is that the beam recombines at a another beamsplitter at the end of the path rather than being reflected directly back towards the initial beamsplitter as in the case of the Michelson Interferometer. We set up the Mach-Zehnder interferometer to have very asymmetric path lengths (a difference of ~ 7 cm) to produce measurable effect in this small interferometer.

Both laser tables are equipped with both amplitude and phase monitors as described above. During the run, we had a limited number of auxiliary channels. Therefore, we would swap between having the antenna, amplitude and phase monitors plugged in. The antenna was always plugged in while the amplitude and phase monitors from the different detectors were swapped. The Interferometer-1 intensity monitor was available for 22% of time while the Interferometer-2 intensity monitor was available for 83% of the time. Both intensity monitors were available for 6% of the time. The Interferometer-1 phase monitor was on for 94% while the Interferometer-2 phase monitor 99%. Both phase monitors were available for 94 %.

II.11 Data Quality

Data quality is determined from two conditions - one set during the data acquisition phase and the other from the environmental monitors.

II.11.1 Data Acquisition Flags

During data acquisition, several criteria were determined to reject a 1 second Fourier transform (or any intermediate steps) from being accumulated with the entire integration. One criterion is a digitizer clipping range, which means that data is flagged if the input voltage range exceeds some predetermined range. The clipping range was set to be within the linear range of the signal detector electronics. Another criterion was set to ensure that we are shot-noise limited during data taking. The measurement from the AC (high frequency) channel is compared to the predicted shot noise amount from the DC channel (low frequency) measurements. If they disagree by more than 20% the data are rejected.

An automated system between the control system of the interferometer and the data acquisition system was developed to inform the data acquisition system to start or stop taking data. This information was based on whether both interferometers were stably operating and the shutters onto the signal detectors were open. Data acquisition concluded when these operating conditions were not met because either the input alignment to the interferometer drifted or there was an external impulse to the system from environmental conditions. Data were removed from segments that were taken either 4 seconds before or 4 seconds after the operating conditions were dropped and reacquired.

Another criterion is that data are rejected if there are no data from the control system. These data are important for determining the calibration outlined in Section II.8.

II.11.2 Auxiliary Channel Vetoes

During the data processing phase, studies of the cross-correlation between the environmental monitors and the signal detectors were used to determine a set of frequency bins that had significant amounts of correlation. The study performed was to identify the correlation between intensity (and phase) monitors with the opposite interferometer's signal detectors . If the coherence was above 95% at any point during the science run, then those individual frequency bins were vetoed and no longer used for scientific processing. Similar criteria were applied for the correlation between the antenna and the signal detectors. Another criterion was to reject frequency ranges less than 100 kHz due to the lack of response from the high frequency chain and seismic noise at low frequencies. The total amount of vetoed bins during this run was less than 1% of the 65,536 frequency bins spanning 0-25 MHz.[42]

II.12 Coherence Tests between Interferometers

We have designed and verified that the Holometer is perfectly in phase. A gravitational wave signal will stretch and squeeze both interferometers by the same amount at the same instance in time. What that corresponds to in terms of the measurement, is a positive correlation along the real axis of the CSD. It is possible that there is an added phase delay introduced due to the separation of the two interferometers. In the design, the separation between the two interferometers is small (0.635 m) compared with the length of the instrument (39.06 m). We have done a series of measurements to test the phase coherence from the input of the interferometers through the digitizers. A test of the interferometer coherence was performed before the science run by phase modulating the input beam before it was sent through the interferometer which converts that signal into a detectable amplitude modulation. A test of signal detector coherence was performed during data acquisition, a continuous 13 MHz LED drive was split and sent through both signal detectors. Another test of signal detector coherence was performed during data acquisition, where an LED was driven with a sine wave across many different frequencies to measure the frequency dependent coherence. This test was designed to simulate the signal strength we were looking for (a small amplitude signal under a bunch of noise), therefore the amplitude of the LED signal was small and a large white noise background was produced with an incandescent bulb. A test of digitizer coherence was performed before data acquisition by driving white noise generated from an amplifier. All of these tests verified that below 15 MHz, the coherence between the interferometers throughout the data acquisition pipeline was >99 %.

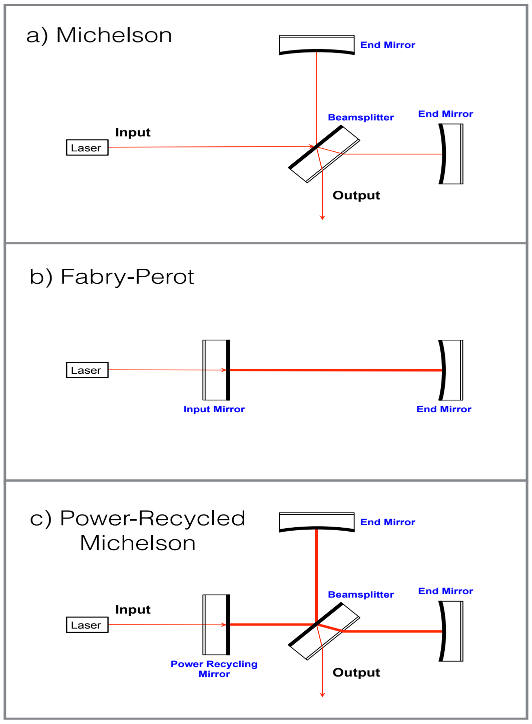

Figure 5 Optical set-up of a simple Michelson Interferometer (panel a), a Fabry-Perot interferometer (panel b) and a Power-recycled Michelson interferometer (panel c).[41] In panel a, the Michelson interferometer has an input laser that interacts with a beamsplitter which reflects half of the light upwards towards an end mirror and transmits the other half of the light towards the end mirror on the right. Both end mirrors reflect light back towards the beamsplitter where the light recombines. Any out-of-phase light exits the interferometer at the bottom of the figure at the output port. Any in-phase light returns back towards the laser. In panel b, the Fabry-Perot interferometer has an input laser that transmits light through the first mirror. The light continues towards the end mirror on the right where it is reflected back towards the input mirror. The light reflects back and forth between the two mirrors. By adjusting the distance of the mirrors to be an integer number of wavelengths, the Fabry-Perot interferometer can be used to resonantly enhance the input laser power. Light exits the interferometer through losses at either mirror. In panel c, the Power-recycled Michelson interferometer combines both the Michelson interferometer and the Fabry-Perot interferometer. In this interferometer, the input laser transmits through the power-recycling mirror, which is essentially the same as the input mirror described for the Fabry-Perot interferometer. The light reflects and transmits off the beamsplitter then reflects back off the end mirrors in the same way as described for the simple Michelson interferometer. The out-of-phase light continues to exit the interferometer in the same way as before. However, the in-phase light is now reflected back into the interferometer by the power-recycling mirror. By adjusting the distance to both end mirrors at the same time, this acts in the same way as described for the Fabry-Perot interferometer. The light is now resonantly enhanced which increases the amount of power in the Michelson interferometer and increases the sensitivity to the difference in arm lengths.

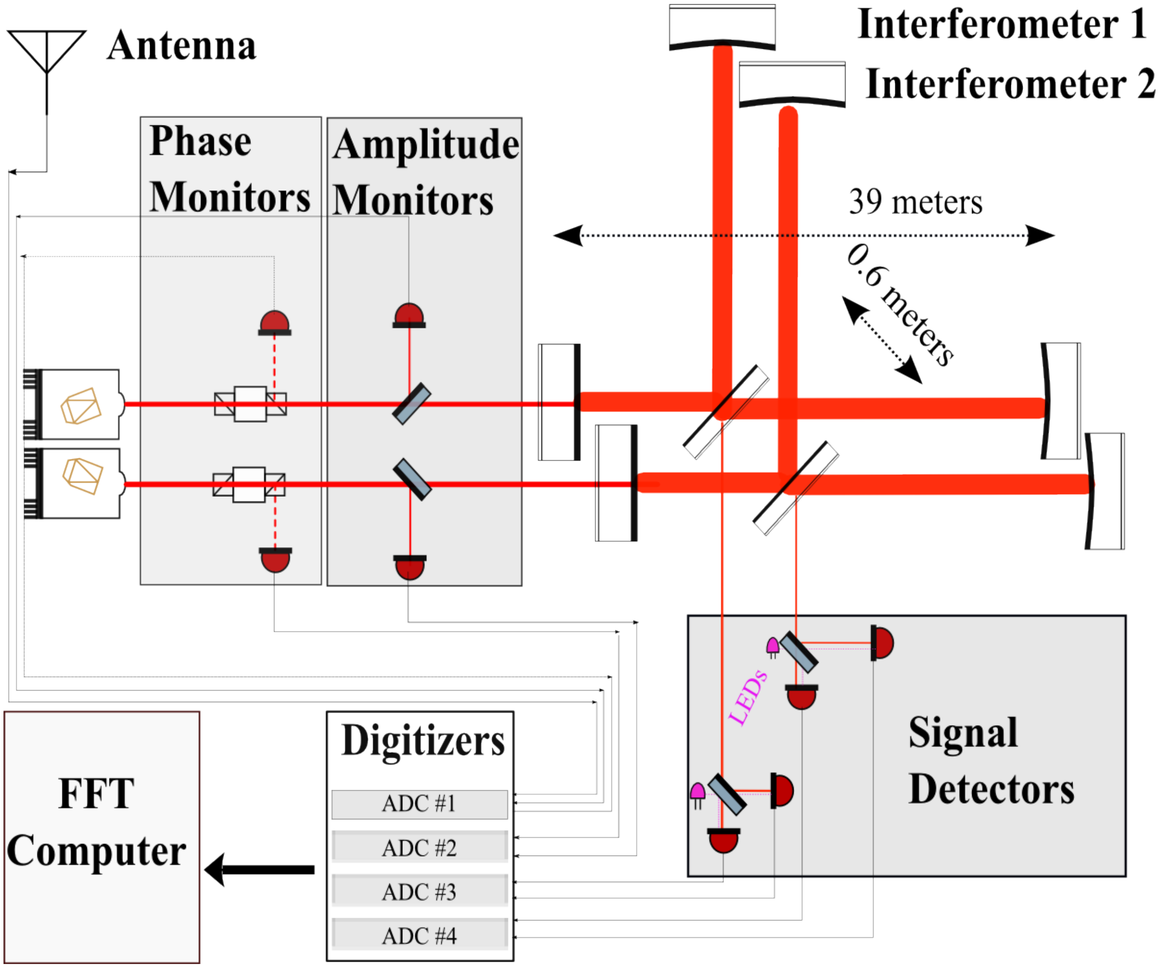

Figure 6 This is a layout of the Holometer from the input lasers to the computers used to process the data. This figure consists of two identical systems of lasers, interferometers and detectors. Additionally, there is an antenna that is used to measure the ambient RF environment. The optical path begins at the laser which is sent towards the power-recycled Michelson interferometers. Less that 1% of the input light is sent into monitors which measure the laser phase and amplitude noise. The light enters the interferometers and follows a path that has been described in Section II.3. The light exits the interferometer and is sent into two signal detectors per interferometer. A 13.06 MHz signal drives two LEDs to measure the coherence between the signal detectors during data acquisition, which will be described in Section II.12. The signals from the interferometer detectors, laser monitors and antenna are sent into 4 separate analog-to-digital digitizers. The antenna was constantly being monitored while the laser monitors were switched throughdue to the limited number of channels available in the digitizers (as described in Section II.10) The signals from each digitizer is sent through a 40 meter optical cable to a 32-core processor computer that performs that Fast-Fourier transform calculations.

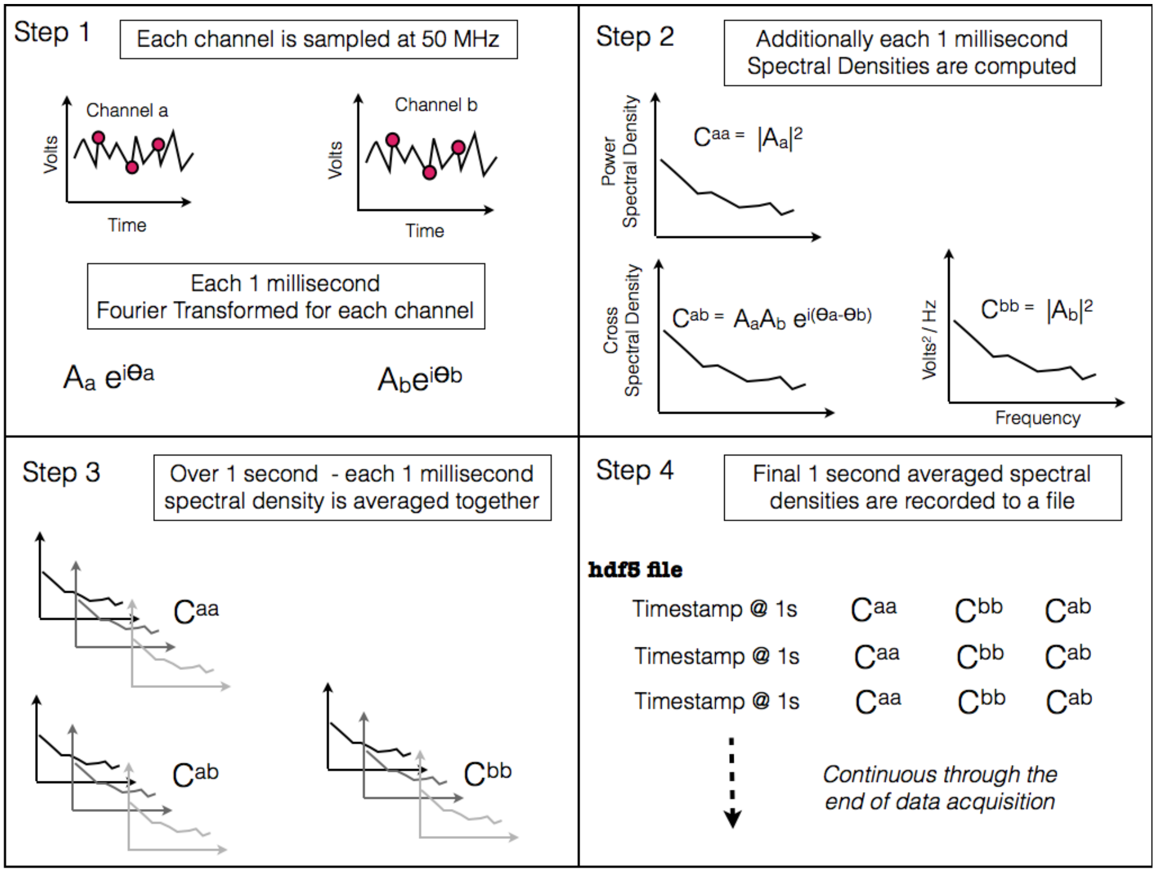

Figure 7 Outline of the data acquisition pipeline from digitizing the detector voltage fluctuations to the information stored in the final data file. This figure outlines the measurements from two channels however this applicable to all 8 channels that are used in the full analysis. In Step 1, the voltage from the detectors in channel a and channel b are sampled at 50 MHz to produce separate time streams of 65,445 individual voltage measurements during 1 millisecond. After 1 millisecond, a Fourier transform is performed on each channel to give the amplitude and phase for each channel, $A_a(f)\, e^{i\theta_a(f)}$ and $A_b(f)\, e^{i\theta_b(f)}$. In Step 2, the power- and cross- spectral densities as a function of frequency are calculated for each channel and have units of V^2/Hz. The power-spectral densities for channel a and b are $C^{aa} = |A_a|^2$ and channel b is $C^{bb} = |A_b|^2$, respectively. The cross-spectral density across channel a and channel b are $C^{ab} = A_a A_b e^{i(\theta_a - \theta_b)}$. In Step 3, each 1 millisecond power and cross-spectral density is averaged together. In Step 4, each of the 1 second power- and cross-spectral density are GPS timestamped at nanosecond precision and recorded throughout the entire integration

CHAPTER III

ANALYSIS-STOCHASTIC GRAVITATIONAL WAVE BACKGROUND

III.1 Stochastic Gravitational Wave Background

To date, direct constraints on the Stochastic Gravitational Wave Background (SGWB) are in the 10^{-9} to 10^{-7} Hz range from pulsar timing arrays and in the 10 to 10^4 Hz range from kilometer scale interferometers. In the 10^6 to 10^7 Hz range, the Holometer will make the first direct limits using decameter scale interferometers.

The constraints by LIGO and Virgo are done by cross-correlating different pairs of interferometers. The first generation of LIGO detectors consisted of 3 kilometer scale interferometers. Two of the interferometers are based at Hanford, Washington (H1-4km and H2 - 2km) while the third interferometer is based in Livingston, Louisiana (L1-4km). Virgo is a 3km interferometer based in Pisa, Italy. The LIGO-Virgo measurement was performed using data while all 3 detectors (H1, L1 and Virgo) were coincidently operating. The LIGO H1-H2 measurement was performed using the two co-located interferometers. This Holometer analysis parallels the measurement using the LIGO H1-H2 pair.

The advantage of utilizing interferometers that are closely separated is the increased sensitivity from phase coherence of the measurement. The pairs such as LIGO H1-L1 or LIGO-Virgo lose sensitivity to SGWB from the decoherence of the signal as it propagates over large distances. What is vitally important for using co-located interferometers is proper accounting of the environmental noise that contaminates the signal.

One of the main differences between LIGO and the Holometer is the scientific frequency range. This plays an important role in what the dominant noise sources are. In the LIGO band, each interferometer is dominated by noise sources such as acoustic, seismic, Newtonian gravitational gradient noise, thermal coating noise, radiation pressure and photon shot noise. In the first generation of the LIGO detectors, they were able to suppress roughly 9 orders of magnitude of noise around 200 Hz with complex pendulum systems for their optics. In the second generation, they were able to gain another order of magnitude in sensitivity. The acoustic, seismic and Netwonian gradient noise is correlated noise while the other noise sources such as thermal coating noise, radiation pressure and photon shot noise are uncorrelated. In the Holometer band, each interferometer is dominated by noise sources such as radio frequency interference (RFI), photon shot noise, laser amplitude and phase noise. The only common source of noise is the RFI contamination which is only in a few narrow frequencies bins while the photon shot noise, laser amplitude and phase noise are uncorrelated.

In the analysis performed both for LIGO H1-H2, a few of the “cleanest” frequency ranges were selected and extensive studies employing the environmental monitors were performed. In this Holometer analysis, a broader range of frequencies can be selected because the only contaminating noise is in narrow frequency bands that are vetoed (Section II.11.2). Another difference to point out between the two experiments is that LIGO stores their time-series data whereas the Holometer only stores frequency domain data as discussed in Section II.7. The initial design of the Holometer was to look for a broadband background noise which did not require analysis in the time domain. Additionally, due to the Holometer's high sampling rate the time series data would produce a few Tb of data per hour. The data acquisition system was developed to do real-time spectral density calculations that significantly decreases the amount of data needed to be stored per hour. Therefore, this analysis will be done exclusively in the frequency domain.

III.2 Cross-correlation technique

Cross-correlation is a powerful technique when searching for signals that are much smaller than the background noise of a single detector. The advantage is that the amplitude of the signal stays constant while the uncorrelated background noise reduces at square root of the number of samples.

If we are looking for a signal, h, that would appear common in two detectors (S_a and S_b), we can write down the measurement in each detector as a linear combination of the signal and the noise for each detector, $\mathcal{N}$.

$$5 - minute S_a = h + \mathcal{N}_a \tag{6}$$

$$S_b = h + \mathcal{N}_b \tag{7}$$

Both the signal and the noise are complex vectors which can be rewritten as the amplitude and the phase ($|h|e^{i\theta_h}$ and $|\mathcal{N}|e^{i\theta_{\mathcal{N}}}$). To compute the cross-correlation, we take the signal from channel a multiplied by the complex conjugate of channel b which is $S_a S_b^*$. Writing out the full expression, we have cross terms between the signal and the noise. These terms are neglected because the signal is much smaller than the noise and this product will contribute much less than the product of the two noise terms. Additionally, there is no expected correlation between the signal and the noise. Taking this into account the cross correlation between the two channels is

$$S_a\, S_b^* \cong |h|^2 + |\mathcal{N}_a||\mathcal{N}_b|e^{i(\theta_{\mathcal{N}_a} - \theta_{\mathcal{N}_b})} \tag{8}$$

If we take the average of the cross-correlation over many samples, N_s, then the average cross correlation expression is

$$< S_a\, S_b^* >_{N_s} \cong \frac{1}{N_s}\,(N_s\,|h|^2 + \sqrt{N_s}|\mathcal{N}_a||\mathcal{N}_b|e^{i(\theta_{\mathcal{N}_a} - \theta_{\mathcal{N}_b})_{N_s}}) \tag{9}$$

where $(\theta_{\mathcal{N}_a} - \theta_{\mathcal{N}_b})_{N_s}$ is the final phase of the noise vectors after many samples. The final result of the average cross-correlation is

$$< S_a\, S_b^* >_{N_s} \cong |h|^2 + \frac{1}{\sqrt{N_s}}|\mathcal{N}_a||\mathcal{N}_b|e^{i(\theta_{\mathcal{N}_a} - \theta_{\mathcal{N}_b})_{N_s}} \tag{10}$$

which demonstrates that with an increased number of samples, you can reduce the effects of uncorrelated noise by a factor $\sqrt{N_s}$.

Figure 8 illustrates what is expressed in Equation 10. If the two detectors are perfectly in phase then the signal will appear only on the real axis (green vector).

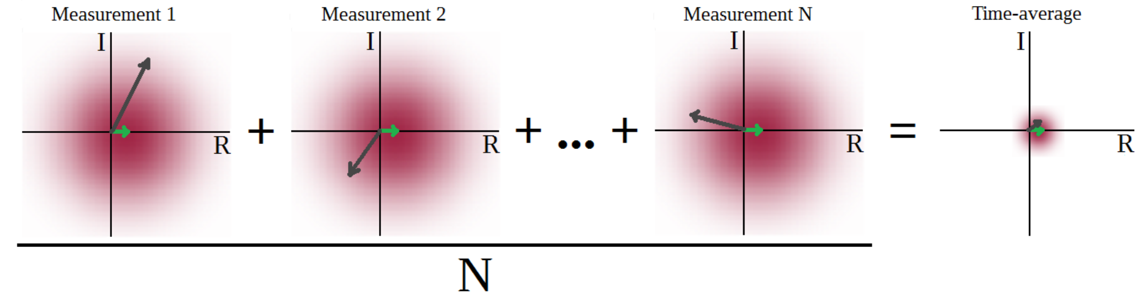

Figure 8 This figure illustrates the advantage of the cross-correlation technique that averages together many measurements which is summarized in Equation 10. Each individual panel represents a measurement in the complex plane with the x axis being the real axis and the y axis being the imaginary axis. The signal, h, is represented by the green vector that is on the real axis. The noise, $\mathcal{N}$, is represented as a black vector . In each subsequent measurement, there is a different noise vector drawn from the Gaussian distribution (red cloud). When all of the different measurements are averaged together (final panel), the resultant noise vector is much smaller than each individual measurement. With continued integration the signal can become much larger than the background noise.

For each measurement, the noise (black vector) is drawn from a Gaussian distribution (red cloud) in the complex plane. When you average together many different measurements of the noise, the resultant noise vector in the complex plane is much smaller than a single measurement of the noise. The signal is a real valued term and remains at the same amplitude throughout the averaging whereas the noise vectors follow a random walk throughout the complex plane that results in a factor of $\sqrt{N_s}$ in the averaging.

Another approach to searching for the signal could be done by looking in a single detector alone. Applying the same steps as above in a single channel, the resulting average value would be

$$< S_a \, S_a^* >_{N_s} \cong |h|^2 + |\mathcal{N}_a|^2 \tag{11}$$

In this approach, there is no added benefit for longer integration times. The noise scales in the same way because you are no longer averaging a complex noise vector. In this case, you would need a very accurate noise model to measure the signal. For example, if you wanted to measure a signal to a precision level of 1% however this signal was 100 times smaller than the noise. This would require an accuracy of the noise model at the 10^{-4} level. In the design and implementation of the Holometer, we use the added benefit of the cross correlation technique to search for weak signals.

III.3 Data analysis pipeline : Stochastic background

Section II.7 described the data acquisition pipeline which takes the data sampled from the different channels and stores the power spectral densities (PSD) and cross-spectral densities (CSD) into an `hdf5` file. Figure 9 outlines the data analysis pipeline that starts at the 1-second integrated spectra and steps through until the fully integrated spectra for the SGWB search or the RA binned data for the narrow-lined search. This figure shows the PSDs and CSDs of two channels though is a general pipeline that is applicable to all 8 channels.

The first step in data analysis pipeline is the final step outlined in Figure 7 which is the 1-second integrated spectra. C^{aa} and C^{bb} are the power spectral densities of channels a and b while C^{ab} is the cross spectral density across those two channels. Explicitly, the $C^{aa} = |A_a|^2$, $C^{bb} = |A_b|^2$ and $C^{ab} = A_a A_b e^{i(\theta_a - \theta_b)}$ where A is the amplitude of the fourier transform and θ is the angle of the vector in the complex plane. The subscript i indicates the 1-second integration.

The next step is to further integrate the data into 5-minute integrated batches. The unweighted average of the PSDs are

$$\mathrm{PSD_{a,5min}} = \sum_{\mathrm{i}}^{\mathrm{5min}} \frac{\mathrm{PSD_{a,i}}}{\mathrm{N_{1sec-spectra}}} \tag{12}$$

$$\mathrm{PSD_{b,5min}} = \sum_{\mathrm{i}}^{\mathrm{5min}} \frac{\mathrm{PSD_{b,i}}}{\mathrm{N_{1sec-spectra}}} \tag{13}$$

where $\mathrm{PSD_{a,5min}}$ and $\mathrm{PSD_{b,5min}}$ are the 5-minute averaged power spectral densities for channels a and b; $\mathrm{PSD_{a,i}}$ and $\mathrm{PSD_{b,i}}$ are the i-th 1-second PSDs for channels a and b; and $\mathrm{N_{1sec-spectra}}$ is the number of 1-second spectra used to create the 5-minute average. Similarly, the 5-minute averaged CSDs are defined as

$$\mathrm{CSD_{axb,5min}} = \sum_{\mathrm{i}}^{\mathrm{5min}} \frac{\mathrm{CSD_{axb,i}}}{\mathrm{N_{1sec-spectra}}} \tag{14}$$

where $\mathrm{CSD_{axb,5min}}$ is the cross-spectral density between channel a and b for 5-minutes of integration ; $\mathrm{CSD_{axb,i}}$ is the i-th 1-second CSD between channels a and b; and $\mathrm{N_{1sec-spectra}}$ is the number of 1-second spectra used to create the 5-minute average.

During this step of integration, the error on the cross-spectral densities are computed in the following way

$$\sigma^2_{\mathrm{axb,5min}} = \frac{\mathrm{PSD_{a,5min}PSD_{b,5min}}}{\mathrm{N_{1sec-spectra}}} \tag{15}$$

where $\sigma^2_{\mathrm{axb,5min}}$ is the error on each 5 averaged minute CSD; $\mathrm{PSD_{a,5min}}$ and $\mathrm{PSD_{b,5min}}$ are the 5 minute integrated PSDs defined in Equation 12 and IV.1.1.

Utilizing the 5-minute integration, the data is further analyzed in two separate ways. The left path in Figure 9 is the path taken for the stochastic gravitational wave background search (SGWB) and the right path is taken for the narrow-lined search which will be described in Section IV.1. An unweighted average of the PSDs was calculated in the same fashion as used for the 5-minute integration

$$\mathrm{PSD_{a,SGWB}} = \sum_{\mathrm{k}}^{\mathrm{130hrs}} \frac{\mathrm{PSD_{a,k}}}{\mathrm{N_{5min-spectra}}} \tag{16}$$

$$\mathrm{PSD_{b,SGWB}} = \sum_{\mathrm{k}}^{\mathrm{130hrs}} \frac{\mathrm{PSD_{b,k}}}{\mathrm{N_{5min-spectra}}} \tag{17}$$

where $\mathrm{PSD_{a,SGWB}}$ and $\mathrm{PSD_{b,SGWB}}$ are the 130 hour averaged power spectral densities for channels a and b; $\mathrm{PSD_{a,k}}$ and $\mathrm{PSD_{b,k}}$ are the k-th 5-minute PSDs for channels a and b; and $\mathrm{N_{5min-spectra}}$ is the number of 5-minute second spectra used to create the 130 hour average.

A weighted average of the CSDs was calculated for the 130 hour integration. This was done to account for variations in the power levels in the interferometers during the full month.

$$\mathrm{CSD_{axb,SGWB}} = \frac{\sum_{\mathrm{k}}^{\mathrm{130hrs}} \mathrm{w_k}\,\mathrm{CSD_{axb,k}}}{\sum_{\mathrm{k}} \mathrm{w_k}} \tag{18}$$

where $\mathrm{CSD_{axb,SGWB}}$ is the cross-spectral density between channel a and b for the full 130 hours of data ; $\mathrm{CSD_{axb,k}}$ is the k-th 5-minute CSD between channels a and b; and

w_k is the weight for the k-th 5-minute CSD. The weights for each individual CSD are the inverse of the variances calculated during the 5-minute integration step

$$w_k = \frac{1}{\sigma^2_{\mathrm{axb,5min,k}}} \tag{19}$$

where w_k is the weight for the k-th 5-minute CSD and $\sigma^2_{\mathrm{axb,5min,k}}$ is the variance stated in Equation 15.

The error on the 130 hour weighted CSD is

$$\sigma^2_{\mathrm{axb,SGWB}} = \frac{1}{\sum_k w_k} \cong \frac{\mathrm{PSD_{a,SGWB}PSD_{b,SGWB}}}{\mathrm{N_{5min-spectra}}} \tag{20}$$

where $\sigma^2_{\mathrm{axb,SGWB}}$ is the error on 130 hour averaged CSD; w_k is the weights on the k-th 5-minute variance; $\mathrm{PSD_{a,SGWB}}$ and $\mathrm{PSD_{b,SGWB}}$ are the 130 hour averaged PSDs for channel a and channel b ; $\mathrm{N_{5min-spectra}}$ is the number of 5-minute spectra were used in the integration. In practice, the error on the 130 hour CSD is equal to the inverse of the sum of the weights $\sum_k w_k$. This accurately represents the changing interferometer power levels over the course of the month. Calculating the error from the fully integrated PSDs, $\left(\frac{\mathrm{PSD_{a,SGWB}PSD_{b,SGWB}}}{\mathrm{N_{5min-spectra}}}\right)$, would slightly overestimate the error because it would not accurately reflect the changing interferometer power level. -

The result of averaging over the 130-hour dataset is in Figure 10. Power spectral densities of each interferometer are shown by the green traces and the weighted averaged cross-spectral density is shown by the blue trace in blue, the error on the cross-spectral density is shown by the black trace. Not only is the black trace the error on the CSD, it is a prediction of where the measured CSD should be given two Gaussian noise source (such as photon shot noise from each interferometer as measured by the PSDs) and the integration time (130 hours). The four orders of magnitude gain in sensitivity exemplifies the advantage of the cross-correlation technique in Section III.2.

III.4 Energy density of Stochastic Gravitational Wave Background

III.4.1 Strain

Strain spectral density is typically the quantity most often discussed in gravitational wave literature, where strain is the change in the arm length over the length of the instrument ($\Delta L/L$). This means transforming the (power- or cross-) spectral density which have units of m^2/Hz to the linear strain spectral density $1/\sqrt{\mathrm{Hz}}$. The first step is to convert from (power- or cross-) spectral density into amplitude spectral density ($\mathrm{m}/\sqrt{\mathrm{Hz}}$) by taking the square root of the power spectral density. The final step is to divide the amplitude spectral density by the length of the interferometer (39.06 m) to get it into strain spectral density.

Figure 11 is the strain spectral density as a function of frequency from 1-13 MHz of the cross-correlation between the two interferometers (blue trace) and the error (black trace). This frequency range will be used in the energy density, Ω_{GW}, analysis described in Section III.4.2. The low frequency cut off for this range was chosen to avoid the correlated laser noise. The high frequency cut off of 13 MHz was a conservative upper limit that ensures the calibration from volts to meters is still valid, avoided the need to account for digitizer sampling decoherence (which becomes at most a 10% effect at 25 MHz), and avoided the 13.06 MHz LED drive signal used during data acquisition to measure the digitizer coherence for all four interferometer signal detectors. Additionally, the concern over the transfer function of gravitational wave signals (see Section IV.1) was relaxed because this search is for a background noise search. Accounting of the high frequency end (above 1.92 MHz) will likely decrease the sensitivity as demonstrated by other gravitational wave detectors[44]. This was not done here though it is entirely possible with future analysis studies.

III.4.2 Energy Density

To compute the energy density, I use a method similar to what was described in the LIGO-VIRGO and LIGO H1-H2 analysis.[32;37;38;36]. LIGO time series equations are translated into what is applicable for the Holometer's frequency domain analysis. The main equations are the energy density Ω, the predicted strain S, and the error σ as a function of frequency.

LIGO computes the energy density for each individual frequency bin as

$$\hat{\Omega}_{\alpha,\mathrm{LIGO}}(f) \equiv \frac{2}{T}\frac{Re(\tilde{s_1^*}(f)\tilde{s_2}(f))}{\gamma(f)S_\alpha(f)} \tag{21}$$

where $\hat{\Omega}_{\alpha,\mathrm{LIGO}}(f)$ is the energy density as a function of frequency for LIGO, T is the duration of data segments used in the FFT [s], Re is the real component of the CSD, $\tilde{s_1^*}(f), \tilde{s_2}(f)$ Fourier transforms of the two different detectors measured in strain [$\mathrm{m}^2/\mathrm{m}^2$] (the product of which is the CSD), γ is the overlap fraction between the two detectors, $S_\alpha(f)$ is the predicted strain for stochastic gravitational wave backgrounds that will be defined below in Equation 23, α is the spectral index which corresponds to either cosmological models ($\alpha = 0$) or astrophysical ($\alpha = 3$) ones.

LIGO is sensitive to both cosmological models of SGWB where sources are generated in the early universe and astrophysical models that are due to unresolved sources stellar remnants from nearby galaxies such as binary black holes, binary neutron stars or other lighter mass ratios binary systems. The term cosmological is for models in the early universe while astrophysical is for models at late times. The Holometer is only sensitive to cosmological models. The comparison will therefore be made between LIGO's measurements for $\alpha = 0$.

LIGO's analysis pipeline computes the energy density for small FFT batches of 900 seconds worth of data, which is further continued throughout the entire integration. The individual frequency bins are averaged together in the range of 80-160 Hz for the cosmological models. Additional averaging was done from 460-1000 Hz though that was used for analysis for astrophysical models. They analyzed data in "clean" regions which is why it was broken up in this way.

The difference with the Holometer pipeline is that Ω_α is calculated for each non-vetoed frequency bin in the 130 hour integrated CSD. This allows for a broader range of frequencies used to measure the energy density. The Holometer version of Equation 21 reduces to

$$\hat{\Omega}_{\alpha,\mathrm{HOLO}}(f) \equiv \frac{Re(\mathrm{Strain}_{\mathrm{IFO1xIFO2}})}{S_\alpha(f)} \tag{22}$$

where $\hat{\Omega}_{\alpha,\mathrm{HOLO}}(f)$ is the energy density for the Holometer, *Re* is the real component of the CSD, $\mathrm{Strain}_{\mathrm{IFO1xIFO2}}$ is the measured strain between interferometer-1 and-2 in [$\mathrm{m}^2/\mathrm{m}^2$] and $S_\alpha(f)$ is the predicted strain for stochastic gravitational wave backgrounds that will be defined below in Equation 23. The separation between the two interferometers is small (0.635 m) compared to the length of the instrument (39.06 m) which makes the overlap fraction, $\gamma = 1$.

The predicted strain for SGWB is defined as

$$S_\alpha(f) = \frac{3H_0^2}{10\pi^2}\frac{1}{f^3}(\frac{f}{f_{\mathrm{ref}}})^\alpha \tag{23}$$

where α is the spectral index dependent on the origin of the SGWB ($\alpha = 0$ in this analysis), H_0 is the Hubble parameter which is a measurement of the expansion rate of the universe ($H_0 = 68$ [km/s/Mpc]) , f is the frequency, f_{ref} is some reference frequency determined by the integrated frequency range ($f_{\mathrm{ref}} = 1$ MHz in this analysis). The predicted strain is used identically for both the Holometer and LIGO analysis.

The measurement error used in LIGO's analysis of the energy density is determined in the following way

$$\sigma^2_{\Omega_\alpha,\mathrm{LIGO}}(f) \approx \frac{1}{2\Delta T}\frac{P_1(f)P_2(f)}{\gamma^2(f)S_\alpha^2(f)} \tag{24}$$

where the $\frac{1}{2}$ comes from using the one-sided power spectral densities for each interferometer (the full PSD has negative values which are unphysical), ΔT is the duration of data segments used in the FFT [s], $P_1(f)$ and $P_2(f)$ is the power-spectral density of LIGO H1 and H2, $\gamma(f)$ is the overlap fraction and $S_\alpha(f)$ is the strain as a function of frequency as defined in Equation 23.

LIGO's error estimate is very similar to the way the Holometer error is defined in Equation 20. The analogous features of this error calculation is the product of the power spectral densities divided by the number of samples N_s, which is directly proportional to the integration time $N_s = T/\tau$ (τ is the length of an individual sample). The factor of $\frac{1}{2\Delta T}$ is to get the error into density units, i.e. dividing by the bandwidth. The error for the Holometer, $\sigma^2_{\mathrm{IFO1xIFO2,SGWB}}$, is already quoted in power spectral density units m^2/Hz.

The error for the Holometer analysis of the energy density is

$$\sigma^2_{\Omega_\alpha,\mathrm{HOLO}}(f) \approx \frac{\sigma^2_{\mathrm{IFO1xIFO2,SGWB}}}{S^2_\alpha(f)} \tag{25}$$

where $\sigma^2_{\Omega_\alpha,\mathrm{HOLO}}(f)$, $\sigma^2_{\mathrm{IFO1xIFO2,SGWB}}$ is the error on the cross-correlation between Interferometer-1 and-2 as defined in Equation 20 and $S_\alpha(f)$ is the strain as a function of frequency as defined in Equation 23.

III.5 MHz Constraint on Stochastic Gravitational Wave Background

Utilizing the full 130 hours of integration, the Holometer constraints on the energy density, Ω_{GW} are plotted in Figure 12. The Holometer 3σ upper limit on the energy density is 5.6×10^{12} at 1 MHz and goes up to 8.4×10^{15} at 13 MHz. This limit is much higher than a value of Ω_{GW}=1, indirect and direct measurements. A value of Ω_{GW}=1 would correspond to the gravitational wave energy density being equivalent to the critical density of the universe. Gravitational waves do not contribute significantly to the total energy budget of the universe, which has been verified through cosmological probes such as the CMB and the large scale structure. Additionally, this direct measurement is much higher that the indirect measurement from BBN. A large contribution of gravitational waves would effect the abundance of neutral atoms and be inconsistent with the current measurements. This Holometer measurement is much higher than other direct measurements such as LIGO-VIRGO and LIGO H1-H2. The reason is a combination of the f^{-3} dependence of the SGWB predictions, more sensitive individual interferometers and longer integration time. In order to be competitive with any of those other experiments, continuous integration would not be the right solution because it will take 10^{24} times longer than the current age of the universe. A major overhaul to the instrument must be done to increase its sensitivity. What this Holometer measurement is capable of constraining is any model that may predict large bursts of gravitational radiation ($\Omega_{GW} \sim 10^{13}$) in a narrow MHz band.

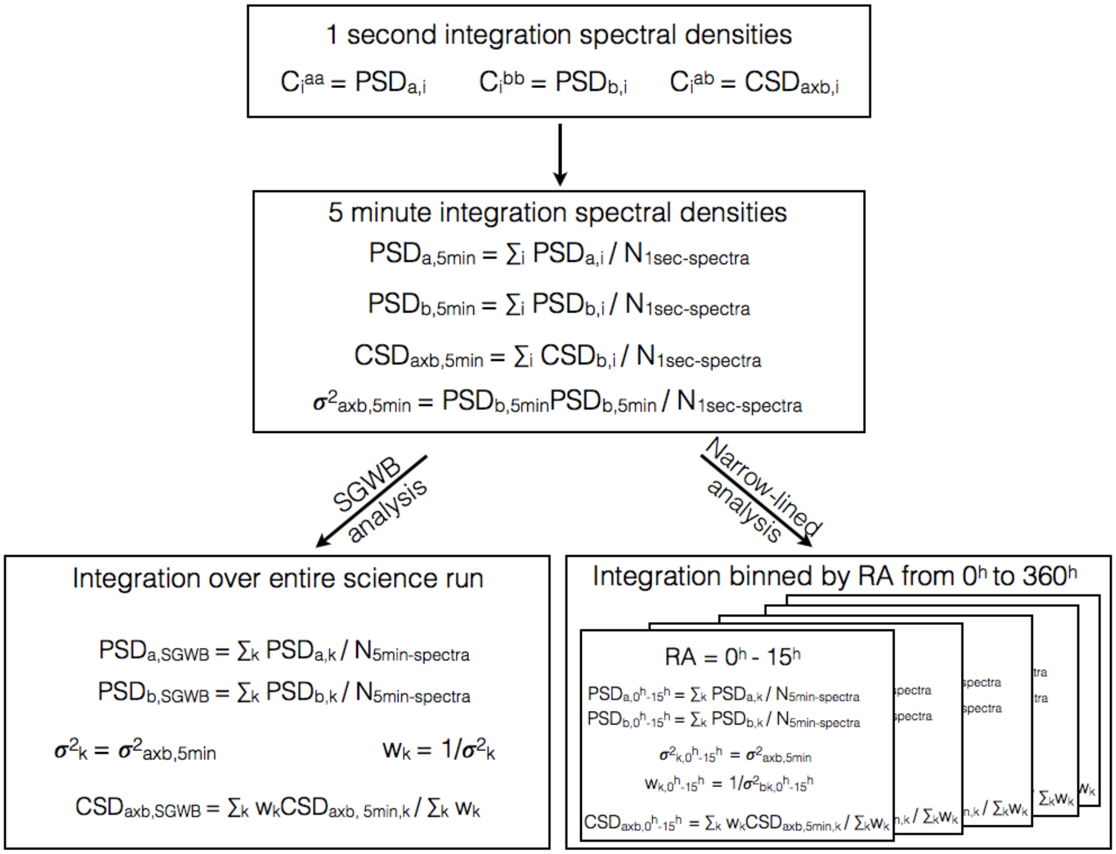

Figure 9 A schematic representation of the data analysis pipeline used in this work. The top panel shows the 1-second integration resolution where C_i^{aa} is the cross correlation of channel a with itself at the i-th 1-second spectra, C_i^{bb} is the cross correlation of channel b with itself at the i-th 1-second spectra. Both C_i^{aa} and C_i^{bb} are the power spectral densities of the respective channels. C_i^{ab} is the cross correlation of channel a with channel b for the i-th 1-second spectra. The details of this integration step are described in Section II.7. The second panel in this figure shows the 5-minute integration resolution. Each of the i-th 1-second spectra are averaged together to give the power- and cross- spectral densities. The noise in the cross-spectral densities, $\sigma^2_{\mathrm{axb,5min}}$, is calculated during this step from the power spectral densities. Utilizing the 5-minute integrated spectra, two different analysis paths were taken. The left panel is used in the stochastic gravitational wave background analysis (SGWB) which averages together the entire 130 hour dataset. The power spectral densities for channel a and b are a straight average of each k-th 5-minute integrated spectra. The cross-spectral densities are weighted averages using the weights calculated in the 5-minute integration step, $1/\sigma^2_{\mathrm{axb,5min}}$ that is applied to each k-th 5-minute CSD. The right panel is used for the narrow-lined analysis that splits the data into 24 separate RA bins. Each individual RA bin is averaged together in the same way as described for the SGWB averaging.

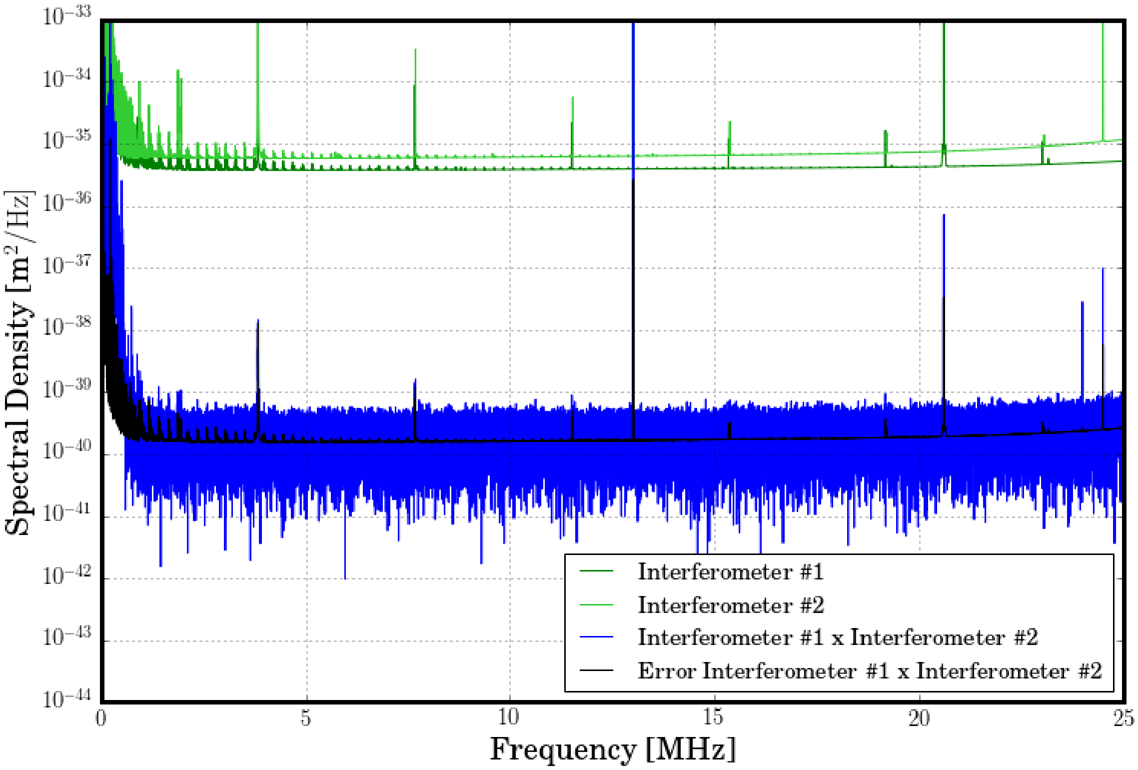

Figure 10 Spectral density as a function of frequency for the full integrated 130-hour dataset from 0-25 MHz. The green traces are the power spectral densities for each of the interferometers (Interferometer-1 = dark green, Interferometer-2 = light green). The blue trace is the magnitude of the cross spectral density between Interferometer-1 and Interferometer-2. The black trace is the statistical uncertainty on the cross-spectral density as predicted from the power spectral densities. All of the features in the individual traces are well understood. Below 200 kHz the dominant noise source is seismic activity. From 200kHz - 1 MHz, the dominant source of noise is laser phase and amplitude noise. From 1 MHz - 25- MHz, the dominant source of noise is photon shot noise. The large spikes at 3.75 MHz and its harmonics are due to laser noise leaking into each interferometer. This happens because the filtering from the Fabry-Perot cavity is insensitive at these frequencies. Another type of noise is the clusters of spikes that begin in the low frequency end (most noticeable at $\sim$ 1 MHz) and have repeated decaying harmonics that are barely noticeable above 15 MHz. These are due to the drumhead modes of the optics in the Michelson interferometer. Studies have verified that each cluster of spikes actually consists of three spikes from the beamsplitter and two end mirrors. This noise source is independent for each interferometer and does not show up in the cross-correlated measurement. The large spike at 13.06 MHz is from two LEDs driven from the same source which is used to verify the coherence of the data acquisition system. The peaks at 22 and 25 MHz are from the phase modulation of the input laser to use for laser frequency stabilization in Pound-Drever-Hall locking. The 4 orders of magnitude gain in sensitivity between the power- and cross- spectral density are from averaging together complex numbers as described in Section III.2.

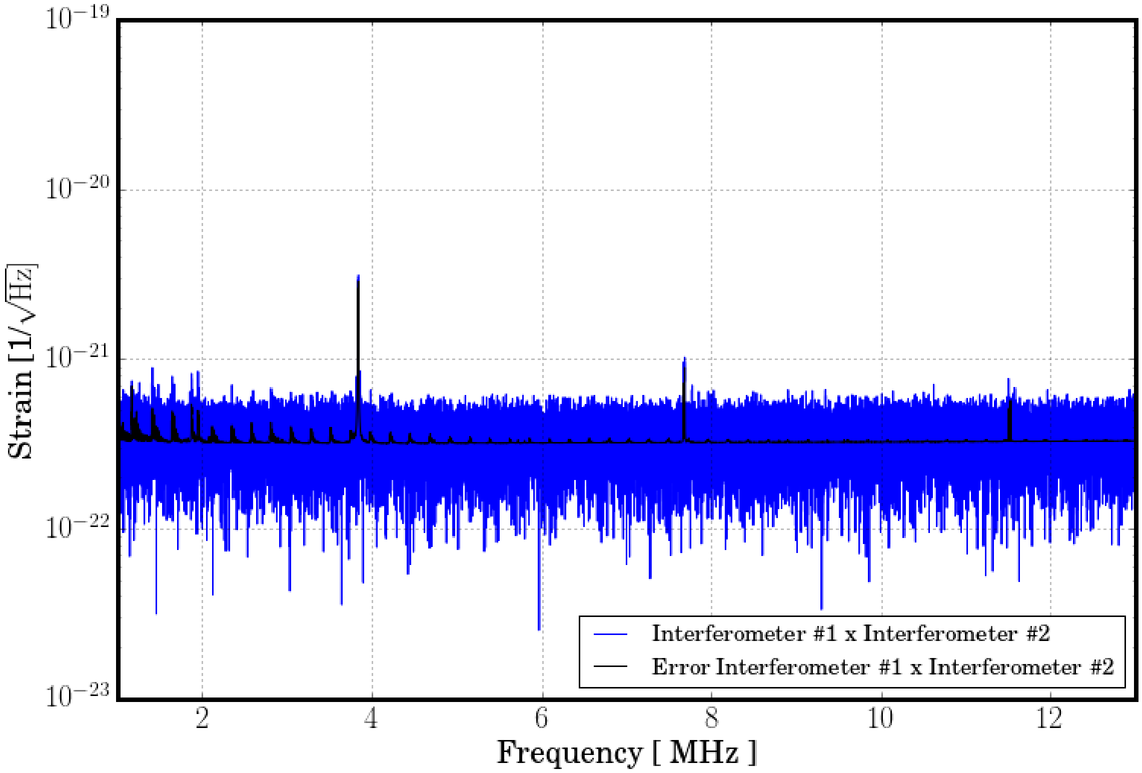

Figure 11 Strain spectral density as a function of frequency from 1-13 MHz. The blue trace is the magnitude of the cross-spectral density that has been transformed into strain units by taking the square root and dividing by the length of the instrument. This is similar to the blue cross-spectral density trace as described in Figure 10. The black trace is the error on the cross-spectral density in strain units. This error was calculated from the individual power spectral densities as described in Section III.3. The frequency range was chosen to be a region dominated by shot noise. The low frequency cut-off of 1 MHz was chosen to avoid contamination from correlated laser noise. The high frequency cut-off was a conservative upper limit chosen to be below the 13.06 MHz LED signal. It is possible to go to higher frequencies though sampling noise enters as a non-negligible source of noise that needs to be accounted for.

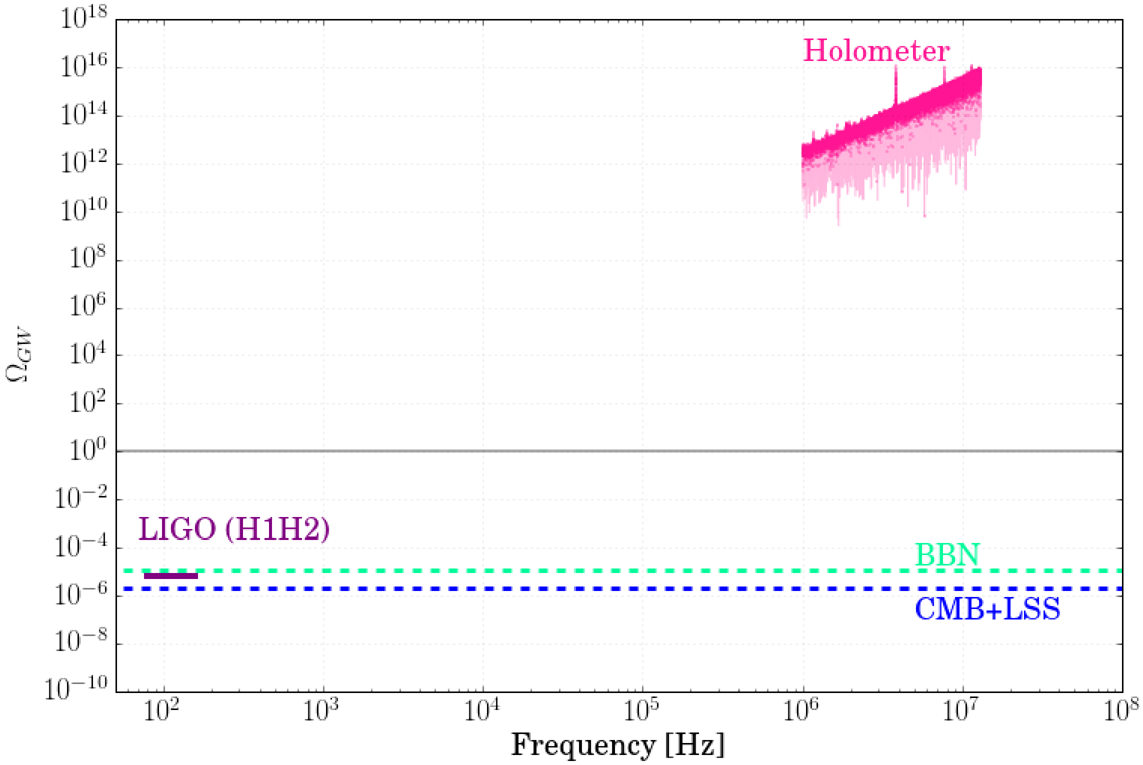

Figure 12 Experimental constraints on the energy density of the stochastic gravitational wave backgrounds, Ω_{GW}, as function of frequency. This is similar to Figure 2 as described in Section I.3.2. For reference, the solid grey line at Ω_{GW}=1 is when the energy density of gravitational waves is equal to the critical density for a spatially flat universe. The Holometer measurement (solid pink line) is the first direct upper limit of MHz gravitational waves in the MHz frequency range. The resulting constraint is much higher than the indirect measurements from BBN (light green dotted line) and CMB (blue dotted line) along with the direct measurements from LIGO H1-H2 (purple). The Holometer measurement is much higher than LIGO's measurement because their individual interferometers are more sensitive, they have longer integration time, and the frequency dependence of the predicted strain, S_α, which scales as f^{-3}. In order to be competitive with these other probes, a major overhaul to the Holometer's sensitivity of the individual interferometers would need to be achieved. Since the Holometer is shot noise limited, the efforts must be invested in increasing the interferometer power.

CHAPTER IV

ANALYSIS-PRIMORDIAL BLACK HOLES

IV.1 Narrow-lined Gravitational Wave Sources

As discussed in the introduction, it is possible to have very narrow-lined frequency gravitational wave sources, such as primordial black holes. We have defined this search to look specifically for monochromatic sources of gravitational waves, which means the sources remain at a constant frequency during the duration of data taking between July 15 - August 15, 2015. This requirement means that the gravitational wave frequency, f_{gw}, must not move into the next bin that is 382 Hz higher during the course of a month. This choice was decided because our data is only stored in the frequency domain, which would make time domain template matching impossible. Additionally, this is only one way of doing the analysis in the frequency domain data and an alternative analysis pipeline is discussed at the end of this chapter. Given this choice of searching for monochromatic sources, we rely on the pointing of the instrument to decide on whether a gravitational wave source exists. If a real source exists, the signal of the strain is the highest at some function of RA and then will decay to zero as the earth rotates away from it. However, if we do not see this pattern then this is an unlikely candidate.

IV.1.1 Data analysis pipeline : Narrow-lined Sources

In this analysis, the frequency range utilized for this study is from 1 to 1.92 MHz. Frequencies below 1 MHz are contaminated by correlated laser phase and amplitude noise and thus were avoided. The upper end of this range was chosen to allow use of the long wavelength approximation, as used by other large scale interferometers such as LIGO. This approximation is valid when the wavelength of the source is 1/4th the wavelength of the detector[45;13;14]. Additional studies for the response function to gravitational wavelengths shorter than this cut off have been done for both ground based gravitational wave detectors and space-based detectors.[46]. In general, the results are that there is a decrease in the sensitivity at shorter wavelengths. For an interferometer of 39.06 meters, the longest full wavelength fits up to 7.68 MHz. Therefore, the long wavelength approximation is valid up to 1.92 MHz in the Holometer's interferometers. Narrow-lined sources may exist above 1.92 MHz however additional modeling of the response function must be employed.

In the long wavelength approximation, the response of the a gravitational wave detector to different polarizations is seen in Figure 13. This response function depends on the opening angle and orientation on the sky relative to the detector. An important feature to note is that gravitational wave detectors are sensitive to incident gravitational radiation from above and below the detector. This contrasts with standard electro-magnetic telescopes which are only sensitive to incident incident radiation from above.

For the total 130-hour dataset, I sorted the data into 24 RA bins as seen in Figure 9

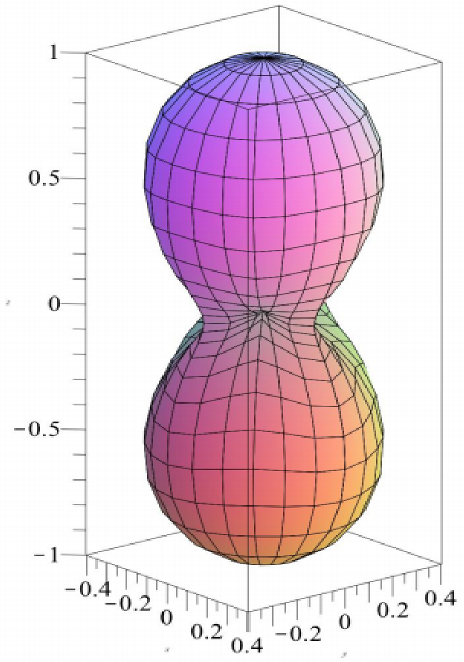

Figure 13 The antenna response function of a gravitational wave detector. Interferometers are omni-directional antennas that are maximally sensitive to gravitational waves incident from both above and below the detector. The sensitivity decreases as incident gravitational waves become aligned with the arms of the detector. The nodes at zero are when the incident waves do not create a response in the interferometer that creates a differential arm length change. Gravitational waves can have two states of polarization (+) and (x). This antenna pattern is the response to both polarizations[47].

where the right branch of the data analysis pipeline was used for the primordial black hole search. At the beginning of each 5-minute segment, I used the UTC timestamp to convert into RA using the python package, `pyephem`, that accounts for the time of year and the Holometer's exact location of longitude = -88.27 and latitude = +41.85. Figure 14 shows the exposure as a function of the RA corresponding to what is directly overhead of the Holometer. Each blue point in Figure 14 maps to the top of the response function in Figure 13 for the Holometer. The variation in exposure time depends on the availability of operators.

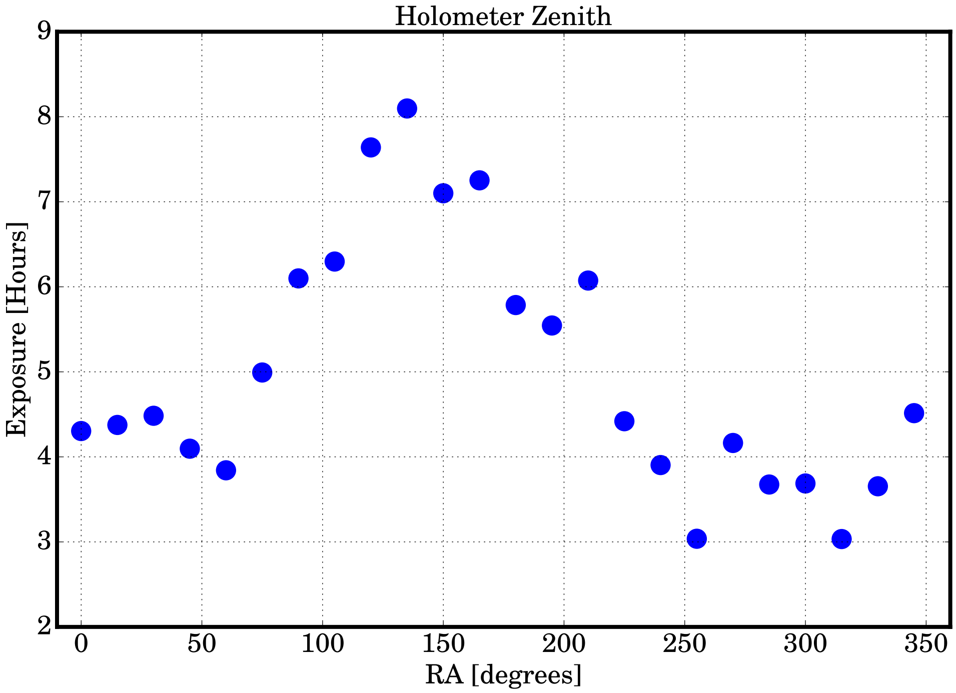

Figure 14 Exposure as a function of RA. The 130-hour dataset was split up into 24 RA bins and each dot represents the exposure time in each RA bin. The modulation in the exposure time is only representative of the amount of available operators. The minimum of $\sim$ 3 hours at RA $\sim$ 260 corresponded to midnight while the maximum at 8.75 hours corresponded to $\sim$ 4pm CST. For a discussion about operations improvements to the duty cycle during this run see Section II.9

Starting at the right branch of the data analysis pipeline in Figure 9, a weighted average for each of the interferometers for each of the 24 RA bins is computed using the following equations :

$$\mathrm{PSD_{a,RA\,bin}} = \sum_{\mathrm{k}}^{\mathrm{T_{RA\,bin}}} \frac{\mathrm{PSD_{a,k}}}{\mathrm{N_{5min-spectra}}} \tag{26}$$

$$\mathrm{PSD_{b,RA\,bin}} = \sum_{\mathrm{k}}^{\mathrm{130hrs}} \frac{\mathrm{PSD_{b,k}}}{\mathrm{N_{5min-spectra}}} \tag{27}$$

where $\mathrm{PSD_{a,RA\,bin}}$ and $\mathrm{PSD_{b,RA\,bin}}$ are averaged power spectral densities for channels a and b, $\mathrm{T_{RA\,bin}}$ is the amount of integration time for that RA bin, $\mathrm{PSD_{a,k}}$ and $\mathrm{PSD_{b,k}}$ are the k-th 5-minute PSDs for channels a and b as defined in Equations 12 and , and $\mathrm{N_{5min-spectra}}$ is the number of 5-minute spectra in the integration time for that bin, $\mathrm{T_{RA\,bin}}$.

A weighted average of the CSDs was calculated for each of the 24 RA bins. This was done to account for variations in the power levels in the interferometers during the full month.

$$\mathrm{CSD_{axb,RA\,bin}} = \frac{\sum_{\mathrm{k}}^{\mathrm{T_{RA\,bin}}} \mathrm{w_k}\, \mathrm{CSD_{axb,k}}}{\sum_{\mathrm{k}} \mathrm{w_k}} \tag{28}$$

where $\mathrm{CSD_{axb,RA\,bin}}$ is the cross-spectral density between channel a and b, $\mathrm{T_{RA\,bin}}$ is the amount of integration time for that RA bin, $\mathrm{CSD_{axb,k}}$ is the k-th 5-minute CSD between channels a and b, and w_k is the weight for the k-th 5-minute CSD. The weights for each individual CSD are the inverse of the variances

$$w_k = \frac{1}{\sigma^2_{\mathrm{axb,5min,k}}} \tag{29}$$

where $\sigma^2_{\mathrm{axb,5min,k}}$ is the variance stated in Equation 15.

The error on weighted CSD for each RA bin is

$$\sigma^2_{\mathrm{axb,RA\,bin}} = \frac{1}{\sum_k^{\mathrm{T_{RA\,bin}}} w_k} \approx \frac{\mathrm{PSD_{a,RA\,bin}PSD_{b,RA\,bin}}}{\mathrm{N_{5min-spectra}}} \tag{30}$$

where $\sigma^2_{\mathrm{axb,RA\,bin}}$ is the error on averaged CSD, $\mathrm{T_{RA\,bin}}$ is the amount of integration time for that RA bin, w_k is the weights on the k-th 130-hour variance, $\mathrm{PSD_{a,RA\,bin}}$ and $\mathrm{PSD_{b,RA\,bin}}$ are averaged PSDs for channel a and channel b 5-minute $\mathrm{N_{5min-spectra}}$ is the number of 5-minute spectra were used in the integration time for that bin ($\mathrm{T_{RA\,bin}}$). In practice, the error on the 130-hour CSD is equal to the inverse of the sum of the weights $\sum_k w_k$. This accurately represents the changing interferometer power levels over the course of the month. Calculating the error from the fully integrated PSDs, $\left(\frac{\mathrm{PSD_{a,RA\,bin}PSD_{b,RA\,bin}}}{\mathrm{N_{5min-spectra}}}\right)$, would slightly overestimate the error because it would not accurately reflect the changing interferometer power level.

In this part of the analysis, it is important to stress that the cross-spectral density is a complex valued function. This means that each frequency bin has both a real and imaginary component. Section III.2 contains a derivation of the cross-correlation technique and Figure 8 illustrates the effect of averaging many measurements in the complex plane that was defined in Equation 10. If there is a real gravitational wave signal then it will lie on the real axis in every instance of the measurement (as seen as the green vector in Figure 8). On the other hand, noise will be drawn from a Gaussian distribution in the complex plane (black vector is the noise and red cloud is the Gaussian distribution). During integration, the repeated measurements reduce the final noise vector (last panel in Figure 8). In the design and implementation of the

Holometer, we have ensured that the measurement of the output of the interferometers are perfectly in phase as described in Section II.12.

Therefore, if a gravitational wave signal did exist it would be measurable in the real component of the CSD for each frequency bin. The real axis would have the signal and the projection of the noise vector onto the real axis. The imaginary axis is a only a measure of the noise (because our instruments are in phases). The imaginary component gives an independent measure of the noise distribution.

The resultant 24 integrated spectra for the real and imaginary components of the CSD are shown below. Figure 15 is the spectral density for the real component of the CSD and Figure 16 is the imaginary component for the first RA bin. All of 24 spectra for real and imaginary components are plotted in Figures 17 and 18.

To verify if the error estimate in Equation 30 is correct, a normalized histogram was compared to a Gaussian distribution. Each individual frequency bin's CSD measurement was normalized by the errors for that frequency bin. The resultant histogram of both the real and imaginary components for the first RA bin is in Figures 19 and 20. The distributions are consistent with a Gaussian distribution described by $\frac{1}{\sqrt{2\pi}} e^{-(x-\mu)^2/2\sigma^2}$ where $\sigma = 1$, $\mu =$ the mean of the error over the 1-1.92 MHz range. This mean values averages to zero because of the even distribution of positive and negative numbers above and below zero. The 24 resultant histograms verify that the noise model is consistent for both the real and imaginary components in each of the RA bins as seen in Figures 21 and 22.

To look for gravitational wave candidates, the ratio of the real component of the

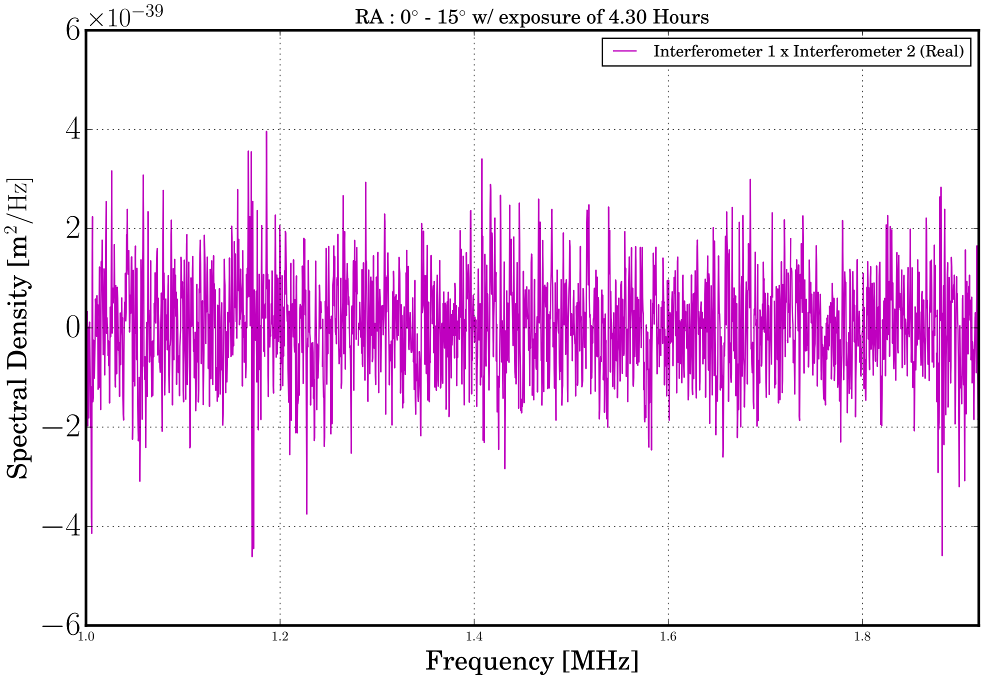

Figure 15 Spectral density as a function of frequency for the real component of the cross correlation between Interferometer-1 and Interferometer-2. After the data is split up into 24 RA bins, this is the resultant integrated spectrum for the first bin in the RA range from 0° to 15° where a total of 4.30 hours of exposure was obtained.

CSD with the CSD error for each individual frequency bin was computed. Additionally, the same ratio was computed for the imaginary component. The imaginary component will not have a gravitational wave signal though it provides is an independent dataset to test the error estimate. Figure 23 shows the real ratio for all 24 RA bins and Figure 24 shows the imaginary ratio. Additionally, Figures 23 and 24 verify that the distribution of this ratio across all 24 bins is consistent with a Gaussian distribution of width 1.

We use a signal-to-noise ratio of 4 as our threshold for candidates since our noise

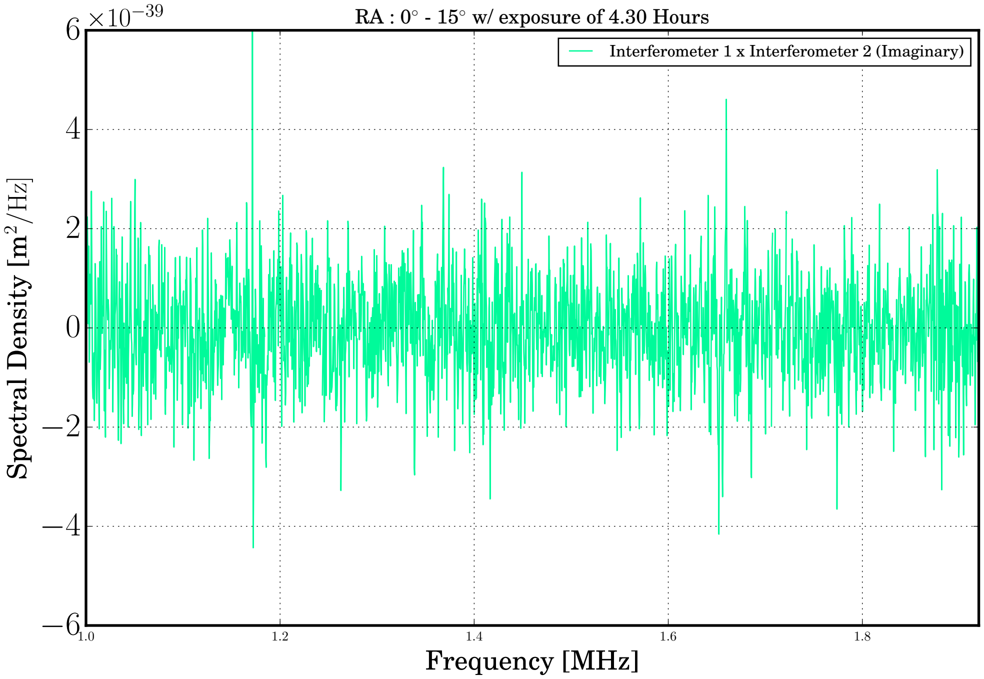

Figure 16 Spectral density as a function of frequency for the imaginary component of the cross correlation between Interferometer-1 and Interferometer-2. This is the similar to Figure 15 though it is the imaginary component of the same complex valued cross-spectral density. This is the resultant integrated spectrum for the first bin in the RA range from 0° to 15° where a total of 4.30 hours of exposure was obtained.

model is very well understood and can be described with a cross-correlation noise model described in Section III.3. This signal-to-noise threshold is lower than LIGO uses for their searches because they operate in regime where there are many more noise source that can potentially inject intermittent spikes of noise that would be consistent with the signals they are looking for.[47]

All the points both above and below 4 sigma are consistent with a normalized Gaussian distribution. There are 2,396 individual frequency bins within the range from 1-1.92 MHz. Accounting for the 24 instances of this ratio, we expect to find

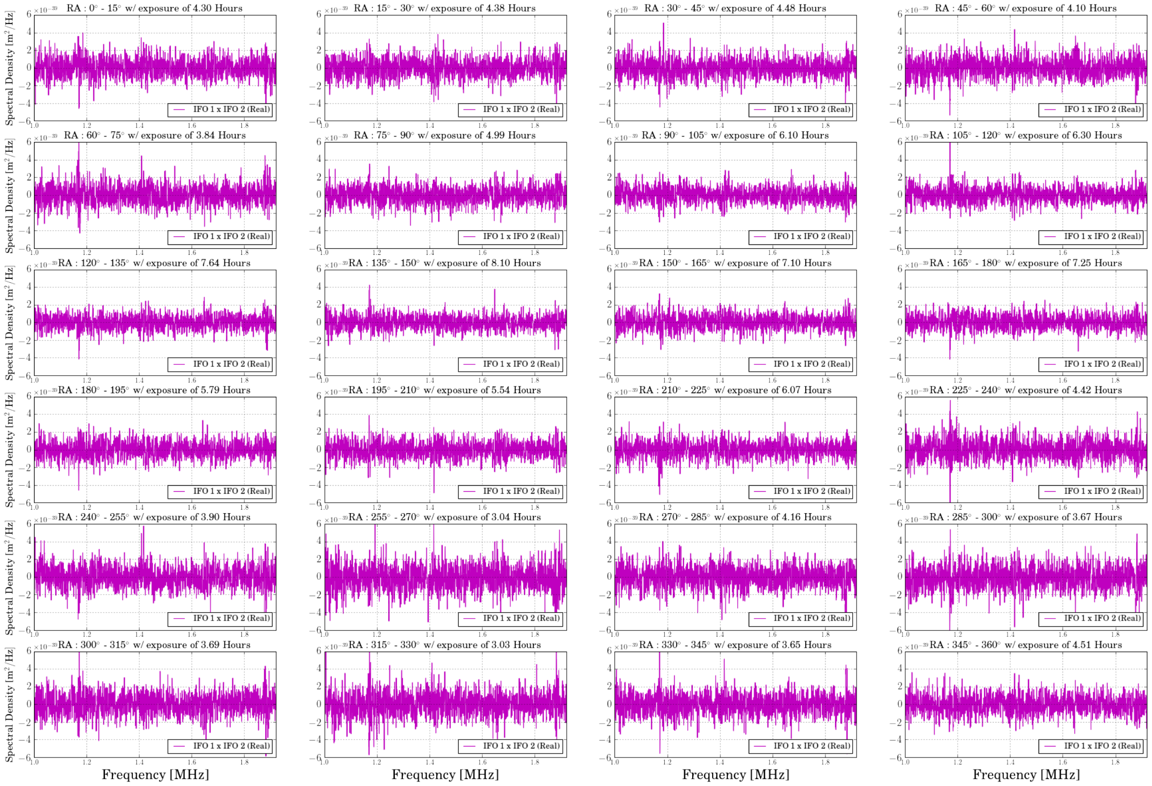

Figure 17 All 24 spectral densities as a function of frequency for the real component of the cross correlation between Interferometer-1 and Interferometer-2. The 130 hours of data were split up into 24 RA bins of width 15° that start at 0° and end at 360°. The exposure time in each bin varied from a minimum exposure time of 3.03 hours to a maximum of 8.10 hours of exposure as seen in Figure 14. The spectra are consistent with one another. The only noticeable variation is a reduction in the fluctuations about zero with increased integration time, which is as expected.

3.64 bins above and below 4 sigma. For the real component ratio, we find there are 4 such points while for the imaginary ratio there are 8 frequency bins within this range. While the real frequency bins are perfectly consistent with my prediction, the imaginary bins were twice as high. We ran a Monte Carlo set of many realizations of 57,504 numbers drawn from a Gaussian and find that the likelihood of getting 8 points higher than $+4\sigma$ or lower than $+4\sigma$ is 3%.

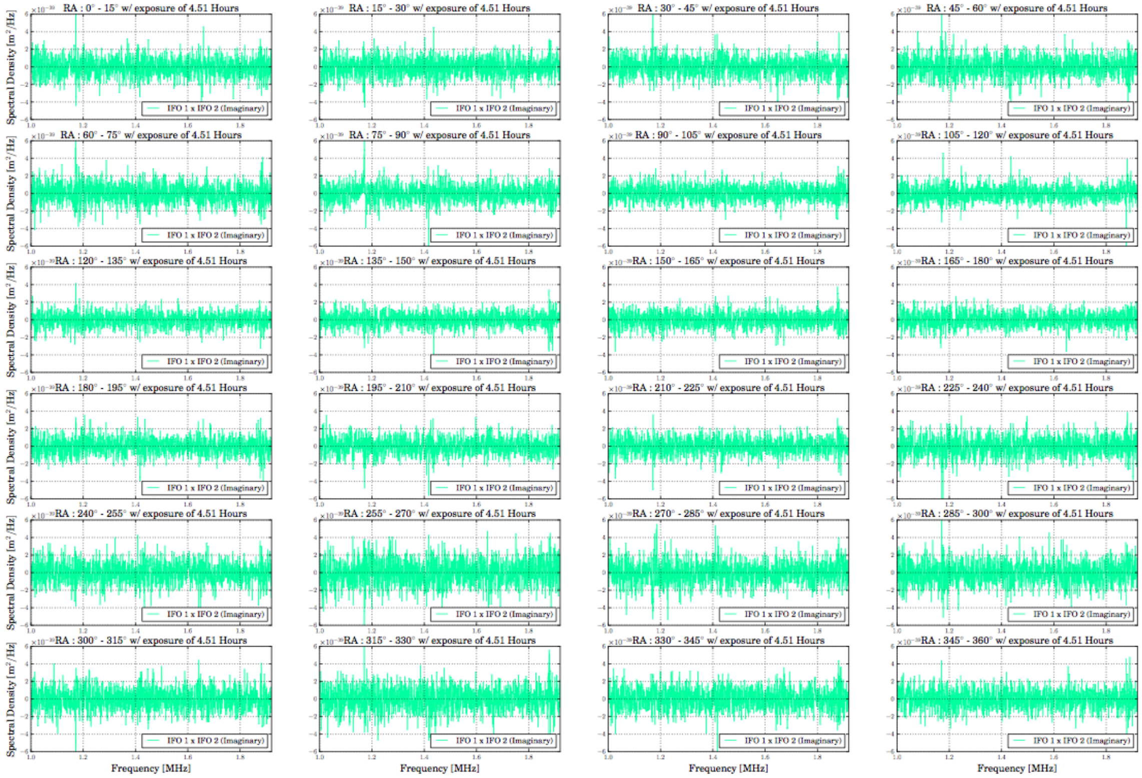

Figure 18 All 24 spectral densities as a function of frequency for the imaginary component of the cross correlation between Interferometer-1 and Interferometer-2. This is the similar to Figure 17 though it is the imaginary component of the same complex valued cross-spectral density. The 130 hours of data were split up into 24 RA bins of width 15° that start at 0° and end at 360°. The exposure time in each bin varied from a minimum exposure time of 3.03 hours to a maximum of 8.10 hours of exposure as seen in Figure 14. The spectra are consistent with one another. The only noticeable variation is a reduction in the fluctuations about zero with increased integration time, which is as expected.

A potential gravitational wave candidate could still be there though would be consistent with a Gaussian distribution. The test is to plot the amplitude of the CSD signal as function of RA. If this is a real astrophysical source then the amplitude of the CSD will be high in a few consecutive RA bins while being consistent with zero in other bins. Candidates with an SNR above 4 in the real component ratio were followed up individually. A total of 2 candidates were looked at individually as seen in Figures 25 and 26. The y axis is in power [m^2] rather than power spectral density [m^2/Hz] because this is a single frequency bin. To convert between the two the bin width of 382 Hz was multiplied to the CSD components.

These two candidates each have a spike in one of the 24 bins though the rest of the bins are consistent with noise centered about zero. Due to the fact that both the real and imaginary components are high at the same bin suggests that there could be some coherent noise (potentially electrical) at that particular hour.

For comparison, one of the imaginary candidates that was flagged above 4 sigma is plotted in Figure 27. It is clear that there was just a random fluctuation in one RA bin while the other RA bins do not exhibit any trends consistent with a gravitational wave signal.

IV.1.2 Results : Primordial Black Hole Binary Constraints

In the Introduction, we discussed mechanism that could produce primordial black holes in the early universe. In this section, we will talk about the Holometer constraints on primordial black hole binary pairs.

A prediction from General Relativity is that two objects orbiting one another will radiate away energy in the form of gravitational radiation. This energy is carried away as gravitational waves. The frequency of gravitational waves, f_{gw}, depends on the mass (that will be described below) and the orbital period P_{orb} ($f_{gw} = \frac{1}{2\,P_{\mathrm{orb}}}$). Additionally, our ability to detect them on earth depends on the distance to the object.

A description of the evolution of a binary system that starts out in Keplerian orbit and radiates away gravitational radiation will be described below. The orbit of the system initially is described by Kepler's Third Law $P_{orb}^2 = \frac{4\pi r^3}{G(m_1+m_2)}$, where P_{orb} is the orbital period, G is the Newtonian gravitational constant and m_1 and m_2 as the masses of the system. As gravitational radiation is lost, the orbital period changes as $\frac{\Delta P_{\rm orb}}{\Delta t} \propto \frac{\Delta f_{gw}}{\Delta t}$. This change is what moves the binary through three stages from inspiral to merger then finally to the ring-down as seen in Figure 28. This figure is the theoretical modeling of the detected gravitational wave signal, GW150914, which was a 28 and 35 $M_\odot$ black hole binary that merged in the LIGO frequency band.[4] To describe the transition between these different stages, the change in the gravitational wave frequency is described by[48;46]

$$\frac{\Delta f_{gw}}{\Delta t} = \frac{96}{5}\frac{c^3}{G}\frac{f_{gw}}{M_c}(\frac{G}{c^3}\pi f_{gw} M_c)^{8/3} \tag{31}$$

where c is the speed of light, G is the Newtonian gravitational constant and M_c is the chirp mass[46]. The chirp mass is a combination of the two masses in the system m_1 and m_2

$$M_c = \frac{(m_1 \times m_2)^{3/5}}{(m_1+m_2)^{1/5}} \tag{32}$$

where M_c is the chirp mass and m_1 and m_2 are each of the masses in the binary system. The chirp mass determines properties of the evolution of the binary system as it radiates gravitational radiation.

This Holometer search is for monochromatic sources, which are binary pairs in the inspiral phase that do not change their gravitational frequency by a detectable amount during our 1 month of data acquisition. Given this constraint, the chirp mass of a binary system that has evolved undetectably in frequency over the time of integration can be found by solving for the chirp mass in Equation 31

$$M_c = (\alpha\, f_{gw}^{-11/3} \frac{\Delta f_{gw}}{\Delta t})^{3/5} \tag{33}$$

where α is the constants $\frac{5}{96}\,\frac{1}{\pi^{8/3}}\,(\frac{c}{G^{1/3}})^5$. To enforce the statement that the binaries do not evolve detectable in frequency over the integration time, we set Δf equal 382 Hz which is the width of each frequency bin and Δt equal to 1 month. This gives the following relationship for chirp mass

$$M_c = (\alpha\, f_{gw}^{-11/3} \frac{382\,\mathrm{Hz}}{1\,\mathrm{month}})^{3/5} \tag{34}$$

In this monochromatic search, Figure 29 shows the maximum masses of the binary systems as a function of frequency from 1 - 1.92 MHz that the Holometer is sensitive to.

To figure out how far out into the universe we can see these objects, we use the horizon distance relationship[48;46]

$$D = \frac{\beta}{\rho}\frac{1}{h^{det}_{f_{gw}}} M_c(\pi f_{gw} M_c)^{2/3}\sqrt{T_{obs}} \tag{35}$$

where β is the constants $\frac{G^{5/3}}{c^4}(\frac{\pi^2}{2})^{1/3}$, ρ is the signal-to-noise ratio, T_{obs} is the observing time and $h^{det}_{f_{gw}}$ is the strain of detector at the frequency f_{gw}. The signal-to-noise ratio used in this search was set to 4 as described in Section IV.1.1.

Figure 30 shows the horizon distance for different values of strain and observing times. The blue trace corresponds to the distance calculated based on the RA bin with the least amount of exposure (3 hrs) and the measured strain value. This trace would correspond to a lower limit on the distance given the amount of observations. The green trace corresponds to the RA bin that has the most amount of exposure (8hrs) which would correspond to a further distance probed. During observations, measurements were taken at all parts of the sky which means that the green trace is representative of how far out we can probe with these binary systems. For reference, the distance from the earth to the international space station (solid gray trace) and the distance from the earth to the moon (dotted trace) are shown. If we had 130 hours of data in each RA bin, how much further would we be able to probe? Given the strain sensitivity in the stochastic gravitational wave background search (Section III.4.1), the distance probed is further though does not quite reach the boundary of the moon's orbit (magenta trace).

We report a null result PBH binaries with masses $8.3 \times 10^{20} - 3.48 \times 10^{21}$ between the earth to the moon. This is the first constraint of primordial black hole binaries in this distance range. As stated in the Introduction, this mass range for primordial black holes is poorly constrained and this offers a new technique to search in this mass range. This is the most conservative estimate for PBH pairs that can be tested with this dataset and alternative analysis paths will be presented below in Section IV.1.3.

IV.1.3 Alternative Analysis paths

One path would be to average together multiple RA hour bins to increase the sensitivity. We computed this for four of the neighboring RA bins to produce new averaged spectra in the same way described in Section IV.1.1. In the new RA bin averaging, the increased sensitivity for the longest integration gains a factor of 1.3 more than the 8 hour integration measurement. This would improve the horizon distance a little though not significant enough to be outside the distance to the moon. Even if each RA bin had the sensitivity equivalent to the sensitivity of integrating 130-hours, this would still not be sufficient to place constraints outside the range of the moon. Once again, the choice to search for monochromatic sources is what constrains the chirp masses so strongly.

On the optimistic end, given the frequency range we operate in one could ask what is the largest chirp masses we would be sensitive to. Assuming that these are Schwarzschild black holes, i.e. non-spinning black holes, in a Keplerian orbit at a separation that corresponds to their inner most stable orbit then the maximum chirp mass derived would be $10^{-3} - 10^{-4}\,\mathrm{M}_\odot$. The increase in the size of these black holes would increase the horizon distance from the earth-moon orbit out to a 50 - 370 kpc ($1.62 \times 10^{21} - 1.13 \times 10^{22}$ m) for 8 hours of integration in each RA bin. This would encompass primordial black hole binary pairs that live within the Milky Way dark matter halo, which extends out to 300 kpc. It is important to note that in order to search for these objects, the time series data would need to be recorded. These binary pairs would radiate gravitational radiation quickly and would change their orbital frequency and move into the next frequency bin in a few nanoseconds. These objects would thus not be able to be searched for in the current data acquisition pipeline however it invites an opportunity for future data acquisition designs.

Another potentially viable path for constraining larger mass binary pairs would be to use this dataset at the 1-second resolution. Rather that starting from the constraint of $\Delta f/\Delta t > 382\,\mathrm{Hz}/1\,\mathrm{month}$, the new constraint would be $\Delta f/\Delta t > 382\,\mathrm{Hz}/1\,\mathrm{s}$. Using this method, the derived masses would be 4 orders of magnitude larger, as shown in Figure 31.

The strain sensitivity would be slightly worse because this measurement would use the instantaneous sensitivity of $5 \times 10^{-21}\,/\sqrt{\mathrm{Hz}}$ rather than the improved limits of integration $7 \times 10^{-22}\,/\sqrt{\mathrm{Hz}}$ for 8 hours of integration. With all that taken into account, the horizon distance would now be out to the distance to Jupiter as seen in Figure 32. To look for these sources, this would require a frequency stacked analysis that is possible with this dataset.

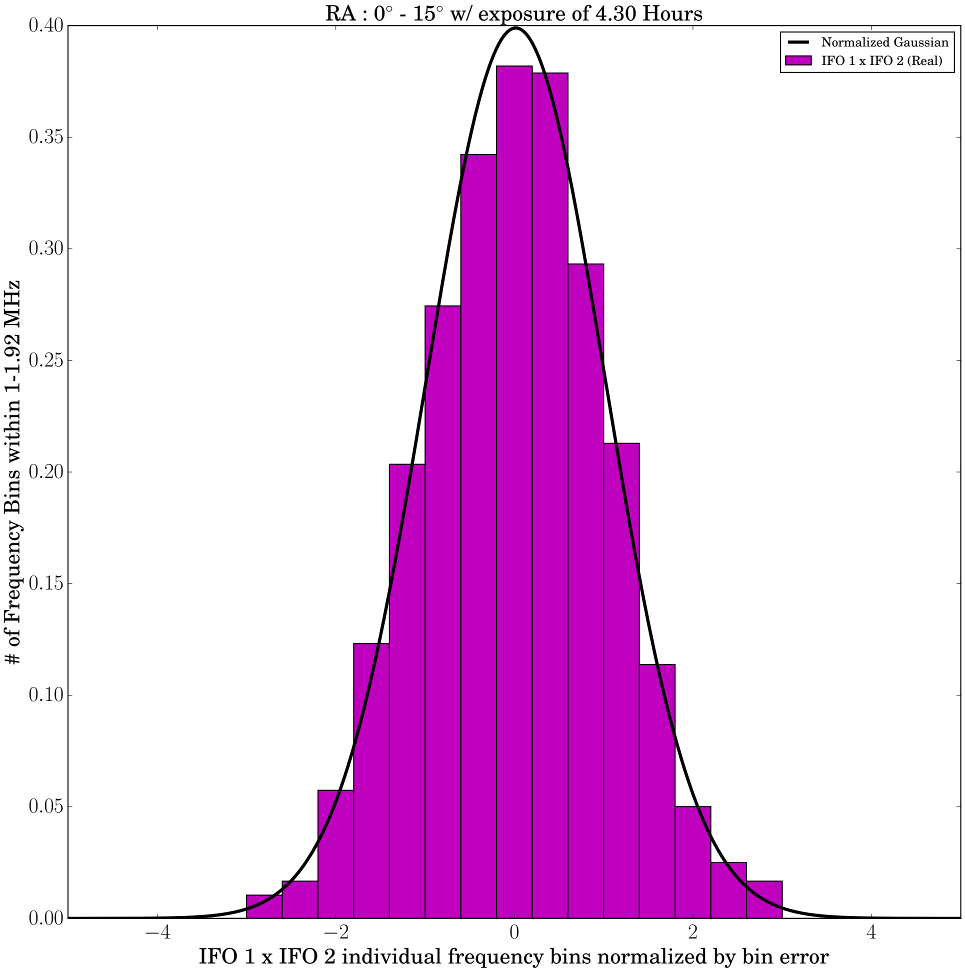

Figure 19 Normalized histogram (pink) of the real component for each individual frequency bin between 1 - 1.92 MHz as compared to a Gaussian distribution (black) of $\sigma = 1$. This is for the first RA bin from 0° to 15° with 4.30 hours of exposure. To generate this distribution, the real component of each individual frequency bin was normalized by the error calculated for that bin $\sigma_{1\mathrm{x}2}(f)$. This illustrates that across this frequency range the noise model of $\sqrt{\frac{\mathrm{PSD}_1\mathrm{PSD}_2}{N_s}}$ is consistent with Gaussian distribution.

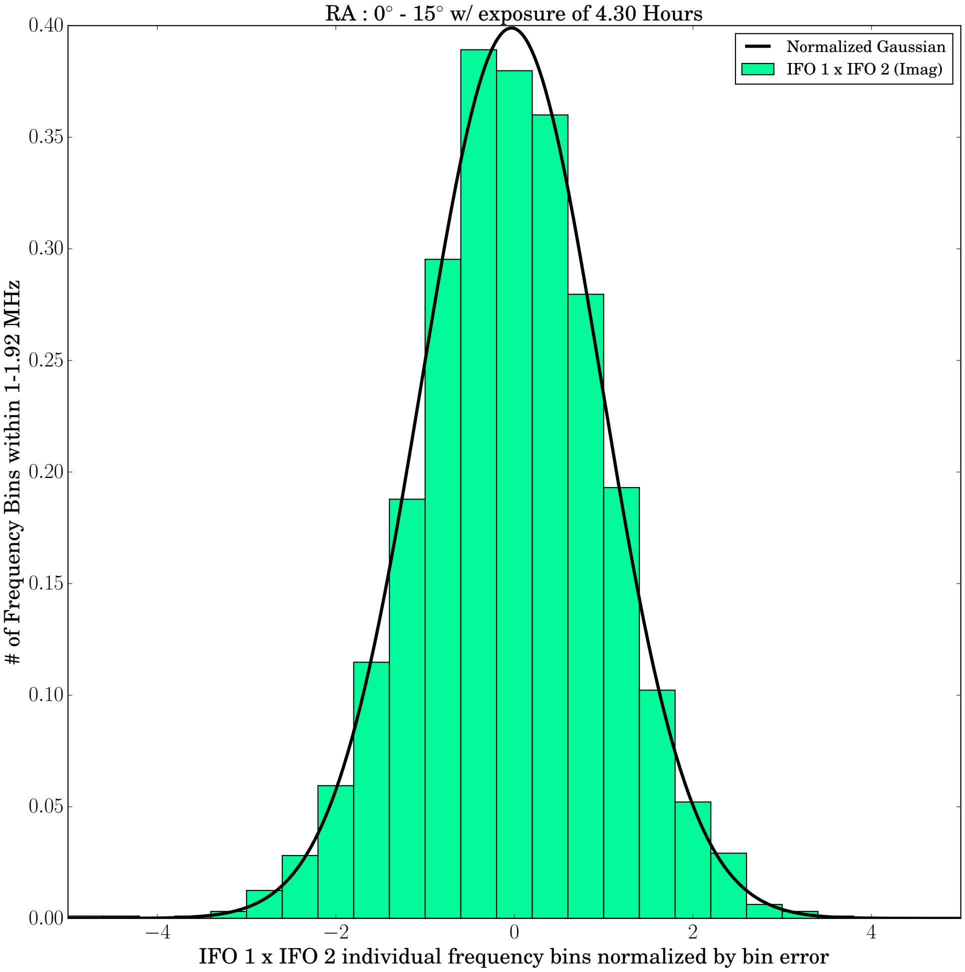

Figure 20 Normalized histogram (green) of the imaginary component for each individual frequency bin between 1 - 1.92 MHz as compared to a Gaussian distribution (black) of $\sigma = 1$. This is for the first RA bin from 0° to 15° with 4.30 hours of exposure. To generate this distribution, the imaginary component of each individual frequency bin was normalized by the error calculated for that bin $\sigma_{1x2}(f)$. This illustrates that across this frequency range the noise model of $\sqrt{\frac{\mathrm{PSD}_1\mathrm{PSD}_2}{N_s}}$ is consistent with Gaussian distribution.

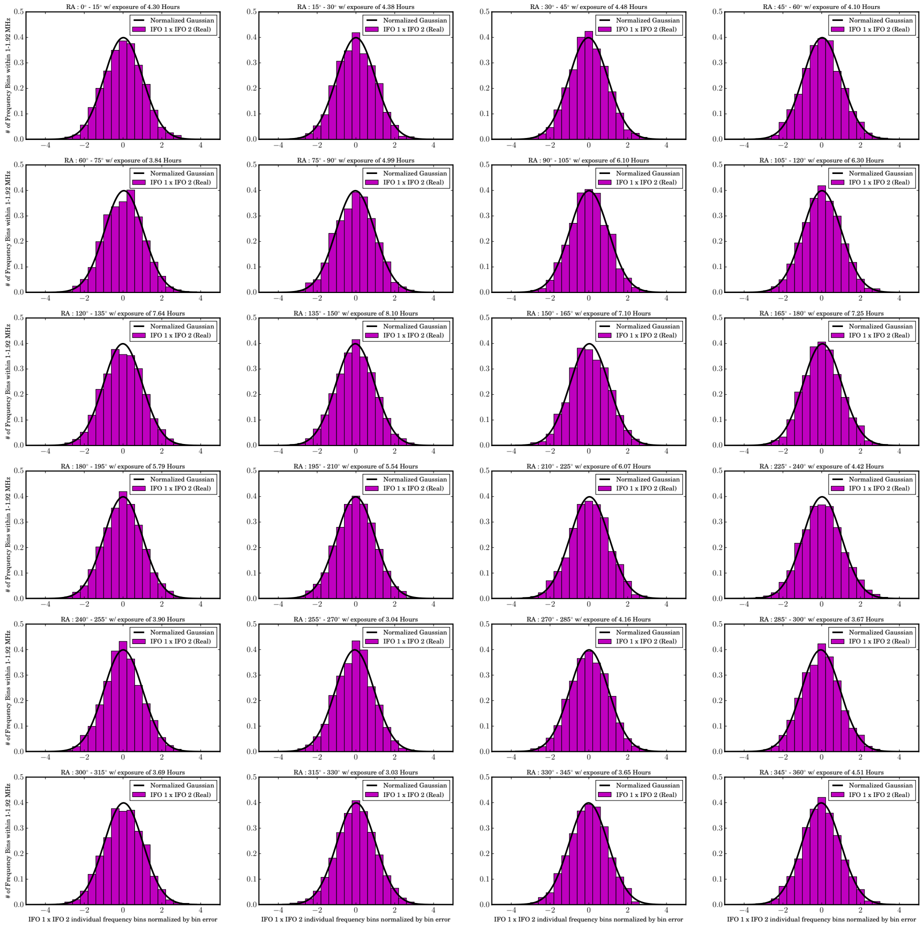

Figure 21 All 24 normalized histograms (pink) of the real component for each individual frequency bin between 1 - 1.92 MHz as compared to a Gaussian distribution (black) of $\sigma = 1$. Figure 19 is the first panel in this grid. This illustrates that all 24 RA bins are consistent with the noise model of $\sqrt{\frac{\mathrm{PSD}_1\mathrm{PSD}_2}{N_s}}$ across this frequency range.

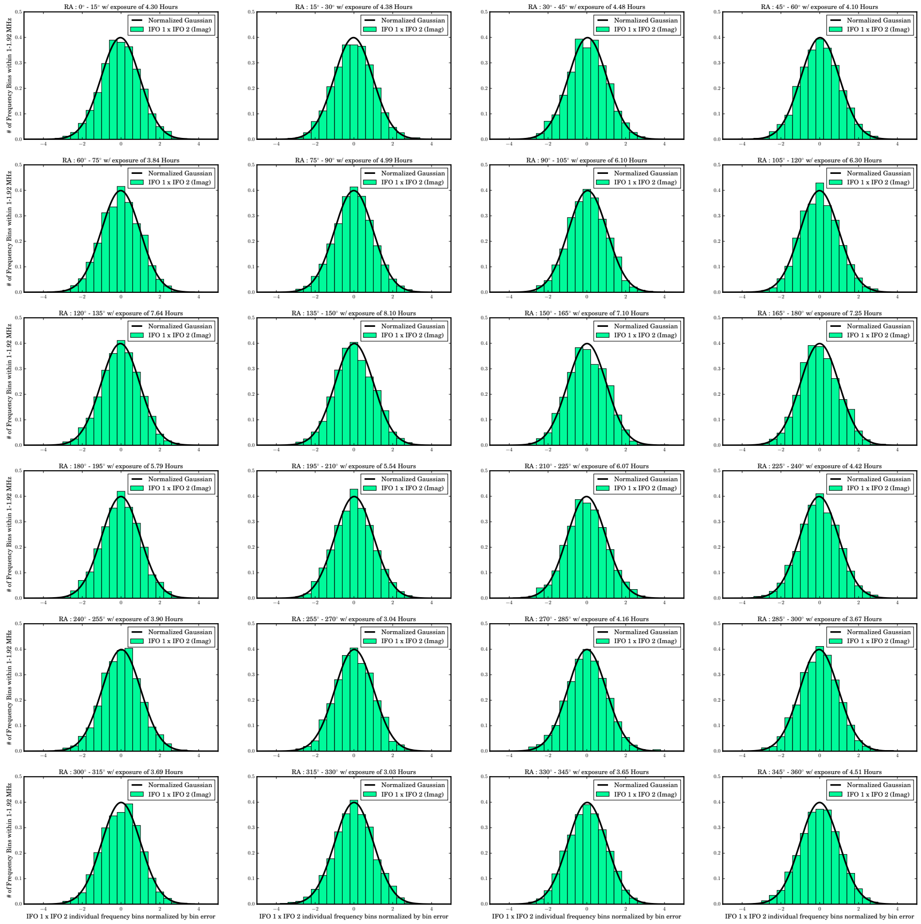

Figure 22 All 24 normalized histograms (green) of the imaginary component for each individual frequency bin between 1 - 1.92 MHz as compared to a Gaussian distribution (black) of $\sigma = 1$. Figure 20 is the first panel in this grid. This illustrates that all 24 RA bins are consistent with the noise model of $\sqrt{\frac{\mathrm{PSD}_1\mathrm{PSD}_2}{N_s}}$ across this frequency range.

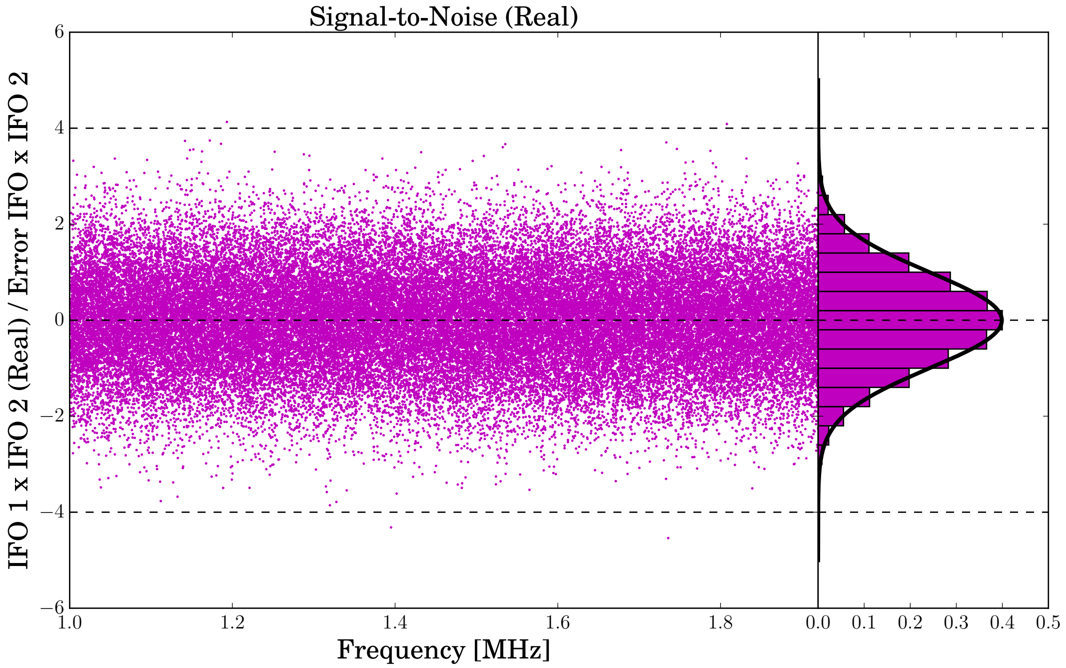

Figure 23 The ratio of the real component of the cross correlation between Interferometer-1 and Interferometer-2 as a function of frequency for all 24 RA bins. Each RA bin consists of 2,396 individual frequency bins within the range from 1-1.92 MHz This includes a total of 57,504 points and the distribution of which is consistent with a Gaussian of $\sigma = 1$ as seen in the vertical panel. The threshold of 4 was selected to search for potential gravitational wave candidates. There are 2 frequency bins above 4σ and 2 frequency bins below 4σ. This amount is consistent with predictions for a Gaussian distribution with 57,504 points. However, it is still possible that one of the frequency bins could be a gravitational wave source and still be consistent with a Gaussian distribution. The two frequency bins above 4σ at 1.19 MHz and 1.80 MHz are selected for follow-up.

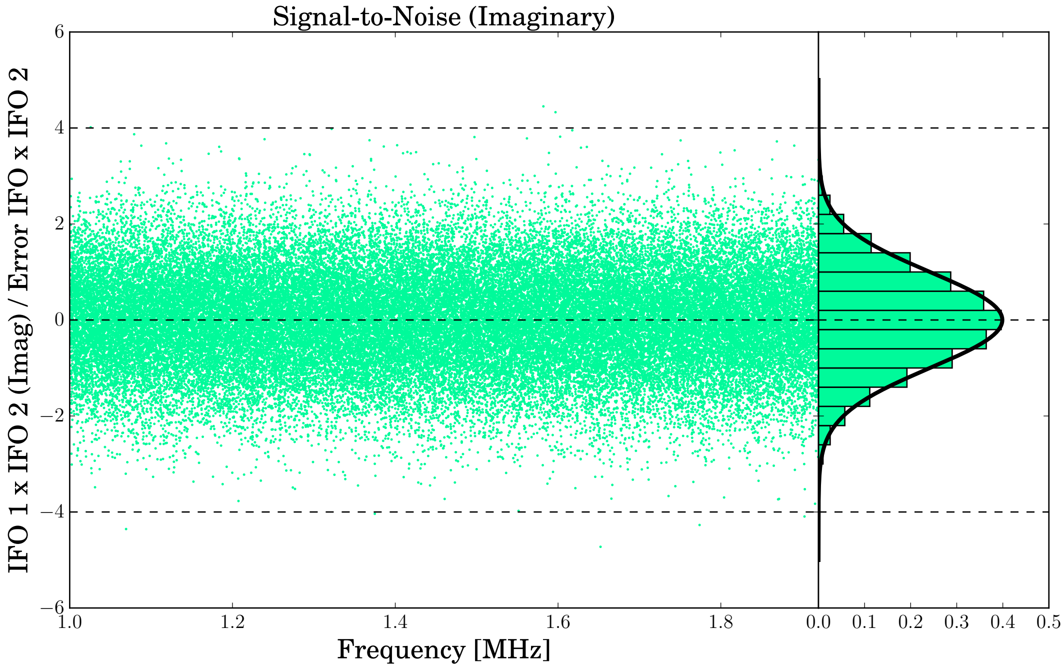

Figure 24 The ratio of the imaginary component of the cross correlation between Interferometer-1 and Interferometer -2 as a function of frequency for all 24 RA bins. Each RA bin consists of 2,396 individual frequency bins within the range from 1-1.92 MHz. This includes a total of 57,504 points which are consistent with a Gaussian of $\sigma = 1$ as seen in the vertical panel. There are 2 frequency bins above 4σ and 6 frequency bins below 4σ. This is slightly higher than predictions for a Gaussian distribution with 57,504 points, however a monte carlo simulation reveals that it is likely to get 8 points 3% of the time.

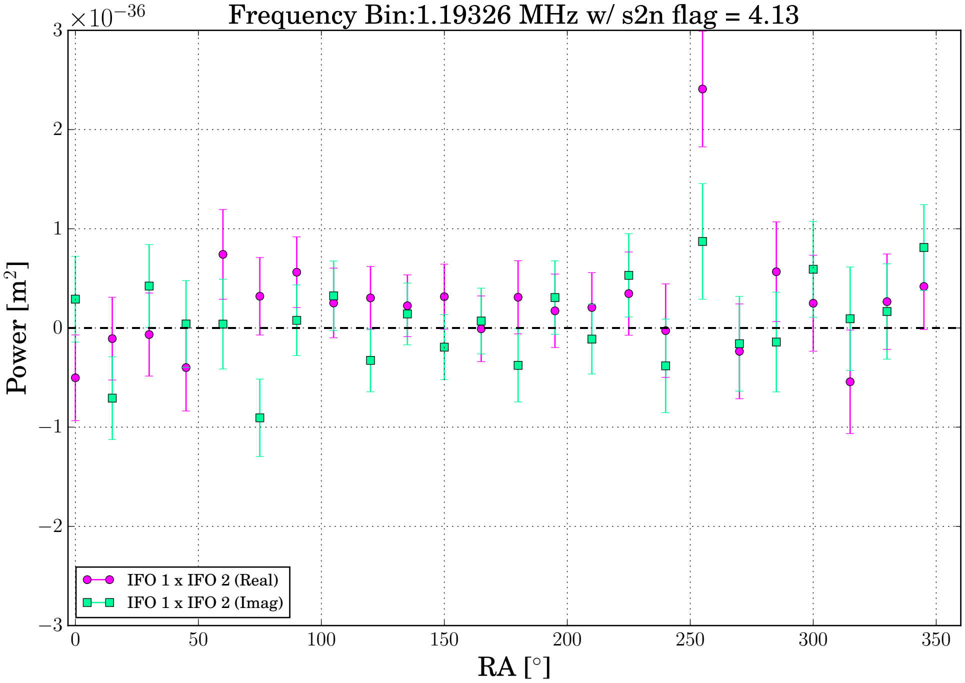

Figure 25 Power as a function of RA for a single frequency bin with a signal-to-noise ratio greater than 4σ. Since this is a single frequency bin, the cross-spectral density values were multiplied by the frequency bin width (382 Hz) to give the amount of length fluctuations in a single bin. The real (pink) and imaginary (green) components of the cross-spectral density are plotted for RA from 0° to 360°. This gravitational wave candidate was selected based on having a strong signal-to-noise value for the real component in one of the 24 RA bins. This candidate was excluded as a potential source because was no excess power in neighboring bins to suggest that this is constant gravitational wave source as defined in this search. The fluctuations of the real and imaginary components about zero are consistent with noise for this frequency bin.

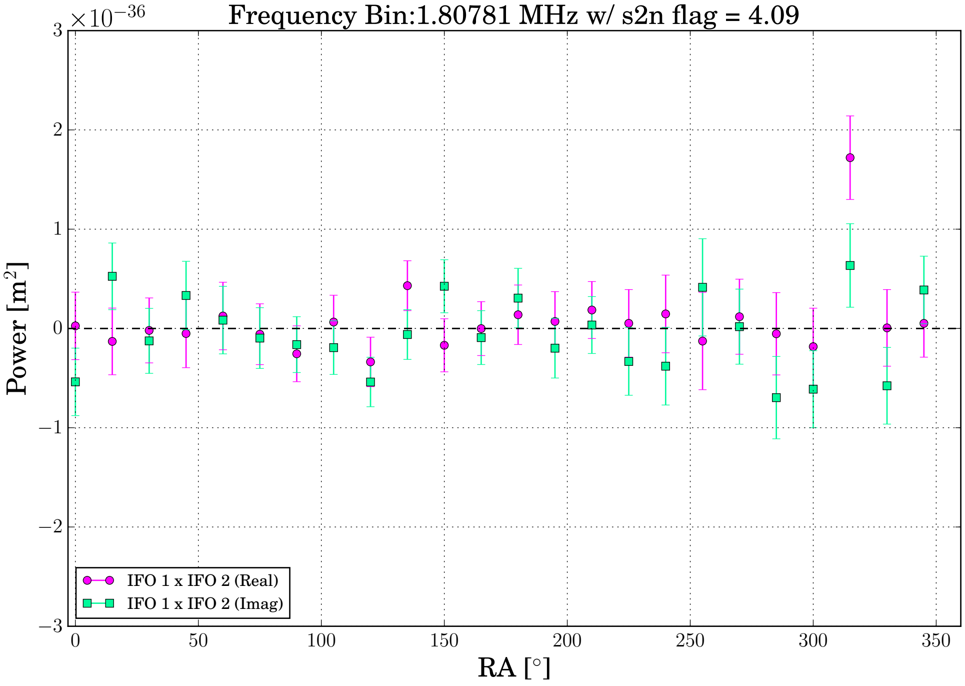

Figure 26 Power as a function of RA for a single frequency bin with a signal-to-noise ratio greater than 4σ. Since this is a single frequency bin, the cross-spectral density values were multiplied by the frequency bin width (382 Hz) to give the amount of length fluctuations in a single bin. The real (pink) and imaginary (green) components of the cross-spectral density are plotted for RA from 0° to 360°. This is another gravitational wave candidate that was selected based on having a strong signal-to-noise value for the real component in one of the 24 RA bins. Additionally, this candidate was excluded as a potential source because was no excess power in neighboring bins to suggest that this is constant gravitational wave source as defined in this search. The fluctuations of the real and imaginary about zero are consistent with noise for this frequency bin.

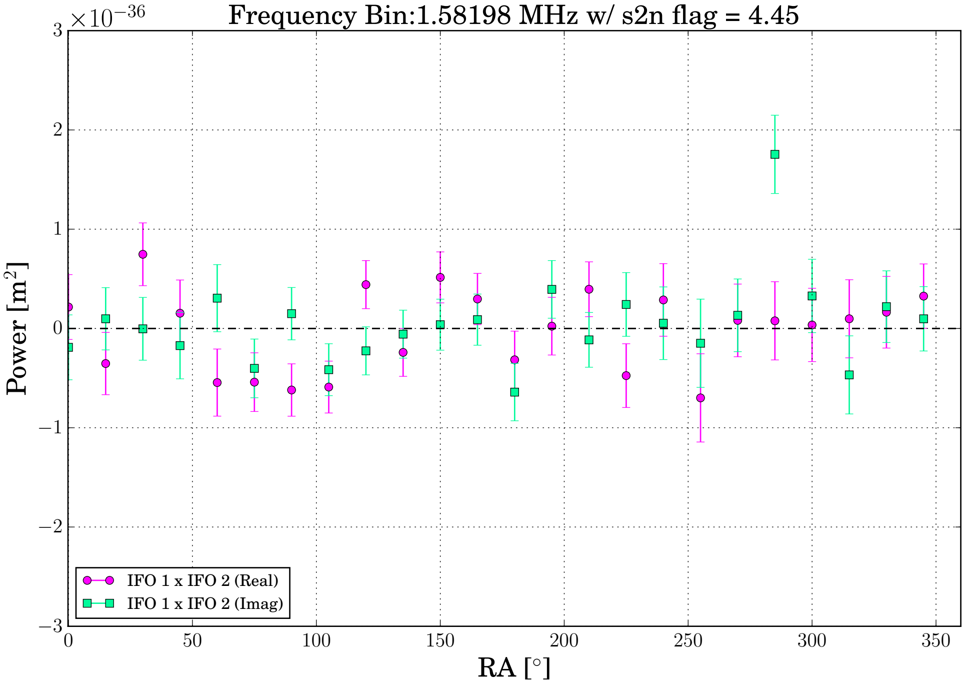

Figure 27 Power as a function of RA for a single frequency bin with a signal-to-noise ratio greater than 4σ. Since this is a single frequency bin, the cross-spectral density values were multiplied by the frequency bin width (382 Hz) to give the amount of length fluctuations in a single bin. The real (pink) and imaginary (green) components of the cross-spectral density are plotted for RA from 0° to 360°. For illustration, the same search criteria as done in Figures 25 and 26 was done to select a candidate with an imaginary component greater than 4σ. In a single RA bin, the imaginary component is high however the rest of the bins are consistent with zero as was the case for the other potential candidates

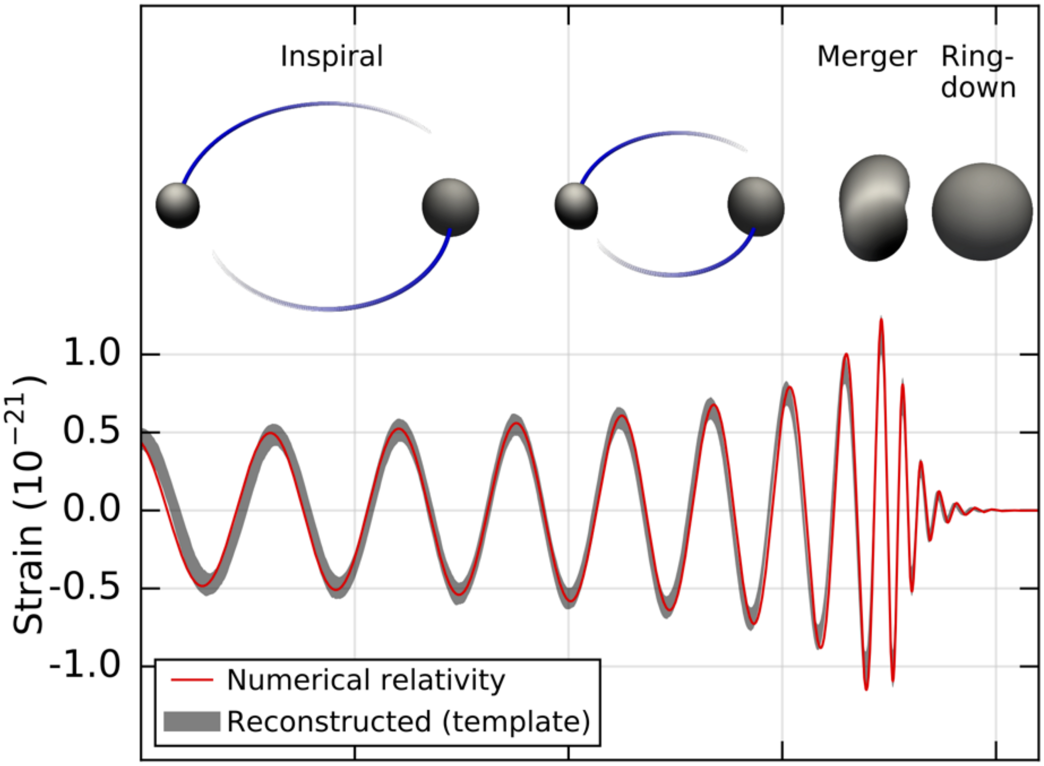

Figure 28 A numerical simulation of the gravitational wave strain signal as a function of time produced from two in-spiraling black holes. There are three phases of a black hole binary merging system depicted in this figure - inspiral, merger and ring-down. During the inspiral phase, the two black holes are in a stable orbit and radiating away gravitational waves at a constant frequency. As the binary system loses energy due to gravitational radiation, the orbit decreases which results in an increase in the gravitational wave strain frequency. The merger phase is when the separation between the two black holes has become so small that the two black holes merge into a final single black hole. The ring-down phase is when the new large black hole has settled down into a new quiescent state that is no longer producing gravitational waves. In this figure, the strain amplitude was based on the 28 $M_\odot$ and 35 $M_\odot$ as discovered by LIGO in September 14, 2015.[4]

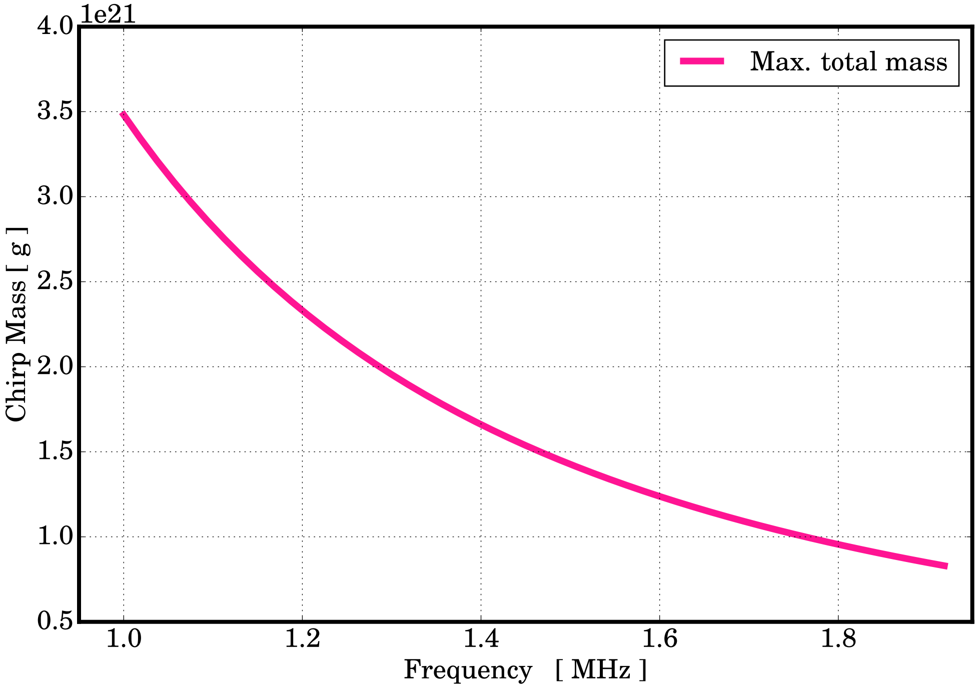

Figure 29 Chirp mass as a function of frequency for the primordial black hole systems accessible in this search. The derived masses of these binary systems enforce the constraint that the binary systems do not have a detectable change in frequency (382 Hz) during the duration of integration (1 month) (Equation IV.1.2). This search is designed to hunt for binaries that would be in the inspiral phase and not merging into larger black holes. This is a conservative analysis choice and alternative analysis paths are discussed in Section IV.1.3.

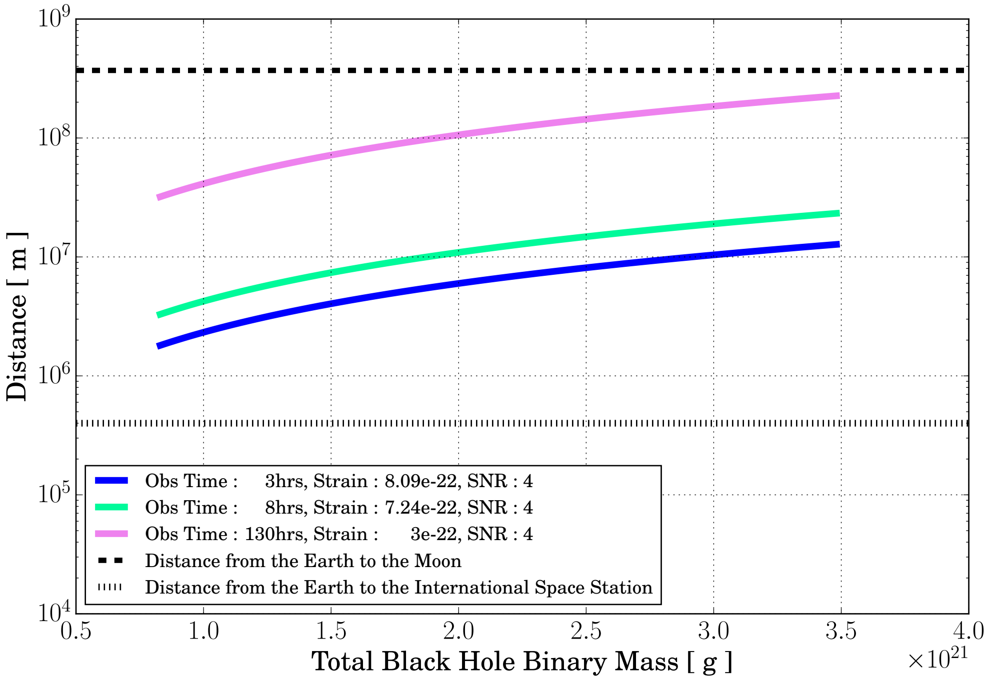

Figure 30 A comparison of different horizon distances as a function of chirp mass for a signal-to-noise threshold of 4. For reference, the dotted line shows the distance from the earth to the International Space station, the dashed black line shows the distance from the earth to the moon. The 130-hour dataset is split up into 24 RA bins that results in a minimum integration time of 3 hours and a maximum integration time of 8 hours. The blue trace represents the minimum distance accessible based on the sensitivity from 3 hours of integration. The green trace shows the increased distance for an integration time of 8 hours. Each frequency bin is measured in all 24 RA bins which means that the furthest distance measured with this analysis is the green trace. The increase in distance for extended integration of 130 hours is shown with the pink trace. The full integrated 130-hour sensitivity from Figure 11 is used to calculate this distance. We find that even with the increased integration time, it is unlikely to search for primordial black hole binaries with this method outside the distance to the moon. In Section IV.1.3, alternative analysis paths could increase the horizon distance out to the distance to Jupiter with this dataset.

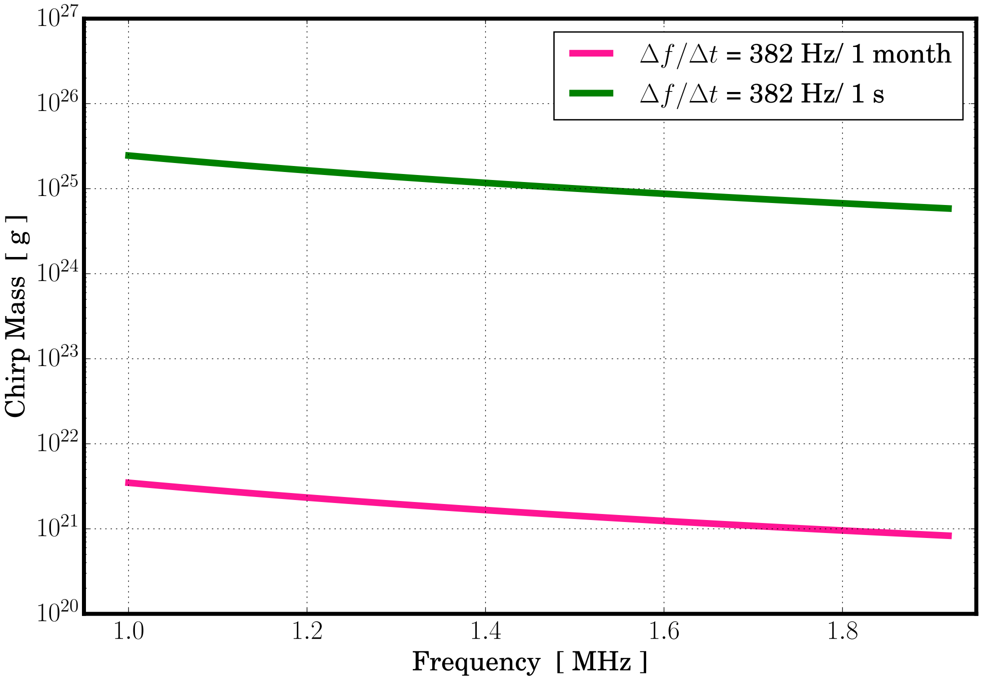

Figure 31 A comparison of the chirp masses as a function of frequency for the analysis used in search (pink trace) as compared to an alternate analysis procedure (green trace). The alternate analysis procedure changes the duration of no detectable frequency change of the system from 1 month (the entire time it took to acquire 130 hours of data) to 1 second (the shortest interval of stored data). These larger binary masses systems would move into the next frequency bin each second. This would require doing a frequency stacked analysis to look for these systems.

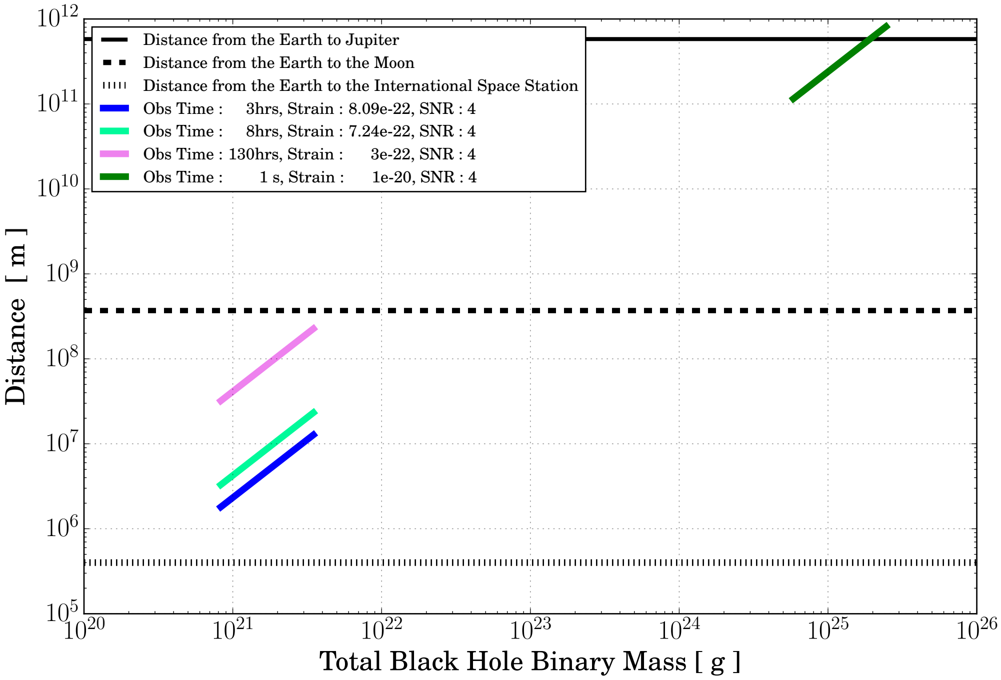

Figure 32 A comparison of the horizon distance as a function of chirp mass for the analysis used in this search (blue and light green traces) as compared to an alternate analysis procedure (dark green trace). For reference, the dotted line shows the distance from the earth to the International Space station, the dashed black line shows the distance from the earth to the moon and the solid black line shows the distance from the earth to jupiter. The alternative analysis procedure increases the distance by four orders of magnitude as compared to an increased distance gain of one order of magnitude from longer integration (pink trace).

CHAPTER V

CONCLUSIONS

The Holometer is a ground-based gravitational wave detector capable of making measurements in a broadband range of frequencies above 1 MHz. The instrument is a pair of power-recycled Michelson Interferometers built at Fermi National Accelerator Laboratory. Each separate yet identical 40 m interferometer has an instantaneous length sensitivity of $2 \times 10^{-18}\mathrm{m}/\sqrt{\mathrm{Hz}}$. This report is on a 130 hour dataset taken between July 15, 2015 - August 15, 2015. With the increased number of samples, this improves the cross-correlated spectral density by two orders of magnitude to $1 \times 10^{-20}\mathrm{m}/\sqrt{\mathrm{Hz}}$ from 1 - 25 MHz.

The first result is the only direct gravitational wave measurement to date of the stochastic gravitational wave background at MHz frequencies. The Holometer 3σ upper limit on the energy density,Ω_{GW}, is 5.6×10^{12} at 1 MHz and goes up to 8.4×10^{15} at 13 MHz. This measurement is much higher than constraints given from the cosmic microwave background and big bang nucleosynthesis that has an integrated Ω_{GW} measurement $\Omega_{\mathrm{GW}}^{\mathrm{CMB}} = 10^{-5}$ and $\Omega_{\mathrm{GW}}^{\mathrm{BBN}} = 10^{-4}$ from $10^{-11} - 10^{15}$ Hz. Measurements from other ground based detectors such as LIGO and VIRGO set a limit of $10^{-4}-10^{-5}$ in the 100 Hz - 10kHz range. The big difference between our measurement and LIGO's is their single detector is 3-5 orders of magnitude more sensitive and when cross-correlating across multiple detectors over their observing season they gain another

2 orders of magnitude. Another big hit to this measurement is that we operate in the MHz frequency range where the predicted spectral shape follows a roughly f^{-3} dependence. This contributes a significant difference between the Holometer and LIGO's measurement.

The second result is there are no detectable non-merging primordial black hole binaries in the mass range $0.7 - 3.5 \times 10^{21}$ g between the earth and the moon. This result was arrived at by splitting the 130 hour Holometer dataset into 24 RA bins from 0°-360° and looking for excess power above the noise for frequencies between 1-1.92 MHz. A signal-to-noise ratio for each of the 2,396 frequency bins between1-1.92 MHz was computed. Two candidate frequency bins with a signal-to-noise $\geq 4\sigma$ for the real component were followed up. None of the candidates exhibited any characteristics consistent with a stationary source that would have the strongest signal while the Holometer faced the source and have no signal while facing away from the source. Enforcing that there is no detectable frequency change occurring over the month of integration that limits the mass range and distance to the sources. Utilizing the same dataset, an alternative analysis path to search for merging primordial black holes can extend the mass range up to $0.6 - 2.5 \times 10^{25}$ g. Additionally, this new mass range would increase the distance range out to Jupiter. The least constrained mass range for primordial black holes[26] is from $10^{20} - 10^{26}$ g and the Holometer dataset opens up a new opportunity to improve measurements in this mass range.

Bibliography

[1] . Einstein, “Die Feldgleichungen der Gravitation,” **Sitzungsberichte der Königlich Preußischen Akademie der Wissenschaften (Berlin)**, 1915.

[2] A. Einstein, “Näherungsweise Integration der Feldgleichungen der Gravitation,” **Sitzungsberichte der Königlich Preußischen Akademie der Wissenschaften (Berlin), Seite 688-696.**, 1916.

[3] A. Einstein, “Über Gravitationswellen,” **Sitzungsberichte der Königlich Preußischen Akademie der Wissenschaften (Berlin), Seite 154-167.**, 1918.

[4] The LIGO Scientific Collaboration and The Virgo Collaboration, “GW150914: First results from the search for binary black hole coalescence with Advanced LIGO,” **arXiv**, pp. 1–20, 2016.

[5] The LIGO Scientific Collaboration, “Astrophysical Implications of the Binary Black-Hole Merger Gw150914,” **arXiv**, vol. arxiv:1602, pp. 1–17, 2016.

[6] The LIGO Scientific Collaboration, “Tests of general relativity with GW150914,” **arXiv**, vol. arxiv:1602, pp. 1–16, 2016.

[7] G. Hobbs, A. Archibald, Z. Arzoumanian, D. Backer, M. Bailes, N. D. R. Bhat, M. Burgay, S. Burke-Spolaor, D. Champion, I. Cognard, W. Coles, J. Cordes, P. Demorest, G. Desvignes, R. D. Ferdman, L. Finn, P. Freire, M. Gonzalez,

J. Hessels, A. Hotan, G. Janssen, F. Jenet, A. Jessner, C. Jordan, V. Kaspi, M. Kramer, V. Kondratiev, J. Lazio, K. Lazaridis, K. J. Lee, R. Manchester, M. Mclaughlin, D. Nice, S. Oslowski, M. Pilia, A. Possenti, M. Purver, S. Ransom, J. Reynolds, S. Sanidas, J. Sarkissian, A. Sesana, and R. Shannon, "The International Pulsar Timing Array project: using pulsars as a gravitational wave detector," **Class. Quantum Grav. Class. Quantum Grav**, vol. 27, no. 27, pp. 84013–10, 2010.

[8] G. H. Janssen, B. W. Stappers, M. Kramer, M. Purver, A. Jessner, and I. Cognard, "European pulsar timing array," **AIP Conference Proceedings**, vol. 983, no. 2008, pp. 633–635, 2008.

[9] Z. Arzoumanian, A. Brazier, S. G. Burke-Spolaor, S. Chamberlin, S. Chatterjee, B. Christy, J. M. J. Cordes, N. Cornish, P. Demorest, X. Deng, T. Dolch, J. Ellis, R. Ferdman, E. Fonseca, N. Garver-Daniels, F. a. Jenet, G. Jones, V. Kaspi, M. Koop, M. Lam, J. Lazio, L. Levin, A. Lommen, D. Lorimer, J. Luo, R. Lynch, D. Madison, M. a. McLaughlin, S. McWilliams, C. M. F. Mingarelli, D. Nice, N. Palliyaguru, T. Pennucci, S. Ransom, L. Sampson, S. A. Sanidas, A. Sesana, X. Siemens, J. Simon, I. Stairs, D. Stinebring, K. Stovall, J. Swiggum, S. R. Taylor, M. Vallisneri, R. van Haasteren, Y. Wang, W. Zhu, M. Kramer, D. J. Champion, M. a. McLaughlin, R. N. Manchester, G. Hobbs, M. Bailes, W. a. Coles, W. van Straten, M. J. Keith, R. M. Shannon, N. D. R. Bhat, A. Brown, S. G. Burke-Spolaor, D. J. Champion, A. Chaudhary, R. T. Edwards,

G. Hampson, a. W. Hotan, A. Jameson, F. a. Jenet, M. J. Kesteven, J. Khoo, J. Kocz, K. Maciesiak, S. Oslowski, V. Ravi, J. R. Reynolds, J. M. Sarkissian, J. P. W. Verbiest, Z. L. Wen, W. E. Wilson, D. Yardley, W. M. Yan, X. P. You, J. S. B. Wyithe, R. M. Shannon, G. Hobbs, R. N. Manchester, A. R. M. Shannon, V. Ravi, L. T. Lentati, P. D. Lasky, G. Hobbs, M. Kerr, S. R. Taylor, C. M. F. Mingarelli, A. Sesana, S. A. Sanidas, A. Vecchio, R. N. Caballero, K. J. Lee, R. van Haasteren, S. Babak, C. G. Bassa, P. Brem, M. Burgay, D. J. Champion, I. Cognard, G. Desvignes, J. R. Gair, L. Guillemot, J. W. T. Hessels, G. H. Janssen, R. Karuppusamy, M. Kramer, A. Lassus, P. Lazarus, K. Liu, S. Osłowski, D. Perrodin, A. Petiteau, A. Possenti, M. B. Purver, P. A. Rosado, R. Smits, B. Stappers, G. Theureau, C. Tiburzi, J. P. W. Verbiest, R. Bott, J. M. J. Cordes, C. Cutler, S. G. Burke-Spolaor, M. Vallisneri, J. Lazio, and W. Majid, "The European Pulsar Timing Array and the Large European Array for Pulsars," **Classical and Quantum Gravity**, vol. 30, no. 22, p. 23, 2013.

[10] F. Jenet, L. S. Finn, J. Lazio, A. Lommen, M. McLaughlin, I. Stairs, D. Stinebring, J. Verbiest, A. Archibald, Z. Arzoumanian, D. Backer, J. Cordes, P. Demorest, R. Ferdman, P. Freire, M. Gonzalez, V. Kaspi, V. Kondratiev, D. Lorimer, R. Lynch, D. Nice, S. Ransom, R. Shannon, and X. Siemens, "The North American Nanohertz Observatory for Gravitational Waves," **arXiv e-prints**, pp. 814–863, 2009.

[11] S. Vitale, "Space-borne gravitational wave observatories," **General Relativity**

and Gravitation, vol. 46, p. 1730, 2014.

[12] The LIGO Scientific Collaboration, "LIGO: the Laser Interferometer Gravitational-Wave Observatory," **Reports on Progress in Physics**, vol. 72, p. 076901, jul 2009.

[13] The LIGO Scientific Collaboration and The Virgo Collaboration, "GW150914: The Advanced LIGO Detectors in the Era of First Discoveries," **arxiv:1602.03838v1**, pp. 1–12, 2016.

[14] The LIGO Scientific Collaboration, "The Sensitivity of the Advanced LIGO Detectors at the Beginning of Gravitational Wave Astronomy," **arXiv**, pp. 1–22, 2016.

[15] C. Bradaschia, R. Del Fabbro, A. Di Virgilio, A. Giazotto, H. Kautzky, V. Montelatici, D. Passuello, A. Brillet, O. Cregut, P. Hello, C. N. Man, P. T. Manh, A. Marraud, D. Shoemaker, J. Y. Vinet, F. Barone, L. Di Fiore, L. Milano, G. Russo, J. M. Aguirregabiria, H. Bel, J. P. Duruisseau, G. Le Denmat, P. Tourrenc, M. Capozzi, M. Longo, M. Lops, I. Pinto, G. Rotoli, T. Damour, S. Bonazzola, J. A. Marck, Y. Gourghoulon, L. E. Holloway, F. Fuligni, V. Iafolla, and G. Natale, "The VIRGO Project: A wide band antenna for gravitational wave detection," **Nuclear Inst. and Methods in Physics Research, A**, vol. 289, no. 3, pp. 518–525, 1990.

[16] F. Acernese, M. Agathos, K. Agatsuma, D. Aisa, N. Allemandou, A. Allocca, J. Amarni, P. Astone, G. Balestri, G. Ballardin, F. Barone, J.-P. Baronick,

M. Barsuglia, A. Basti, F. Basti, T. S. Bauer, V. Bavigadda, M. Bejger, M. G. Beker, C. Belczynski, D. Bersanetti, A. Bertolini, M. Bitossi, M. A. Bizouard, S. Bloemen, M. Blom, M. Boer, G. Bogaert, D. Bondi, F. Bondu, L. Bonelli, R. Bonnand, V. Boschi, L. Bosi, T. Bouedo, C. Bradaschia, M. Branchesi, T. Briant, A. Brillet, V. Brisson, T. Bulik, H. J. Bulten, D. Buskulic, C. Buy, G. Cagnoli, E. Calloni, C. Campeggi, B. Canuel, F. Carbognani, F. Cavalier, R. Cavalieri, G. Cella, E. Cesarini, E. C. Mottin, A. Chincarini, A. Chiummo, S. Chua, F. Cleva, E. Coccia, P.-F. Cohadon, A. Colla, M. Colombini, A. Conte, J.-P. Coulon, E. Cuoco, A. Dalmaz, S. D'Antonio, V. Dattilo, M. Davier, R. Day, G. Debreczeni, J. Degallaix, S. Deléglise, W. D. Pozzo, H. Dereli, R. D. Rosa, L. D. Fiore, A. D. Lieto, A. D. Virgilio, M. Doets, V. Dolique, M. Drago, M. Ducrot, G. Endrczi, V. Fafone, S. Farinon, I. Ferrante, F. Ferrini, F. Fidecaro, I. Fiori, R. Flaminio, J.-D. Fournier, S. Franco, S. Frasca, F. Frasconi, L. Gammaitoni, F. Garufi, M. Gaspard, A. Gatto, G. Gemme, B. Gendre, E. Genin, A. Gennai, S. Ghosh, L. Giacobone, A. Giazotto, R. Gouaty, M. Granata, G. Greco, P. Groot, G. M. Guidi, J. Harms, A. Heidmann, H. Heitmann, P. Hello, G. Hemming, E. Hennes, D. Hofman, P. Jaranowski, R. J. G. Jonker, M. Kasprzack, F. Kéfélian, I. Kowalska, M. Kraan, A. Królak, A. Kutynia, C. Lazzaro, M. Leonardi, N. Leroy, N. Letendre, T. G. F. Li, B. Lieunard, M. Lorenzini, V. Loriette, G. Losurdo, C. Magazzù, E. Majorana, I. Maksimovic, V. Malvezzi, N. Man, V. Mangano, M. Mantovani, F. Marchesoni, F. Marion, J. Marque, F. Martelli, L. Martellini, A. Masserot, D. Meacher, J. Meidam,

F. Mezzani, C. Michel, L. Milano, Y. Minenkov, A. Moggi, M. Mohan, M. Montani, N. Morgado, B. Mours, F. Mul, M. F. Nagy, I. Nardecchia, L. Naticchioni, G. Nelemans, I. Neri, M. Neri, F. Nocera, E. Pacaud, C. Palomba, F. Paoletti, A. Paoli, A. Pasqualetti, R. Passaquieti, D. Passuello, M. Perciballi, S. Petit, M. Pichot, F. Piergiovanni, G. Pillant, A. Piluso, L. Pinard, R. Poggiani, M. Prijatelj, G. A. Prodi, M. Punturo, P. Puppo, D. S. Rabeling, I. Rácz, P. Rapagnani, M. Razzano, V. Re, T. Regimbau, F. Ricci, F. Robinet, A. Rocchi, L. Rolland, R. Romano, D. Rosińska, P. Ruggi, E. Saracco, B. Sassolas, F. Schimmel, D. Sentenac, V. Sequino, S. Shah, K. Siellez, N. Straniero, B. Swinkels, M. Tacca, M. Tonelli, F. Travasso, M. Turconi, G. Vajente, N. van Bakel, M. van Beuzekom, J. F. J. van den Brand, C. Van Den Broeck, M. V. van der Sluys, J. van Heijningen, M. Vasúth, G. Vedovato, J. Veitch, D. Verkindt, F. Vetrano, A. Viceré, J.-Y. Vinet, G. Visser, H. Vocca, R. Ward, M. Was, L.-W. Wei, M. Yvert, A. Z. Żny, and J.-P. Zendri, "Advanced Virgo: a second-generation interferometric gravitational wave detector," **Classical and Quantum Gravity**, vol. 32, no. 2, p. 024001, 2015.

[17] K. A. Strain, B. Allen, P. Aufmuth, C. Aulbert, S. Babak, R. Balasubramanian, B. W. Barr, S. Berukoff, A. Bunkowski, G. Cagnoli, C. A. Cantley, M. M. Casey, S. Chelkowski, D. Churches, T. Cokelaer, C. N. Colacino, D. R. M. Crooks, C. Cutler, K. Danzmann, R. Davies, R. J. Dupuis, E. Elliffe, C. Fallnich, A. Franzen, A. Freise, S. Gossler, A. Grant, H. Grote, S. Grunewald, J. Harms, G. Heinzel, I. S. Heng, A. Hepstonstall, M. Heurs, M. Hewitson,

S. Hild, J. Hough, Y. Itoh, R. Jones, S. H. Huttner, K. Kawabe, C. J. Killow, K. Koetter, B. Krishnan, V. Leonhardt, H. Lueck, B. Machenschalk, M. Malec, R. A. Mercer, C. Messenger, S. Mohanty, K. Mossavi, S. Mukherjee, P. Murray, S. Nagano, G. P. Newton, M. A. Papa, M. Perreur-Lloyd, M. Pitkin, M. V. Plissi, V. Quetschke, V. Re, S. Reid, L. Ribichini, D. I. Robertson, N. A. Robertson, J. D. Romano, S. Rowan, A. Ruediger, B. S. Sathyaprakash, R. Schilling, R. Schnabel, B. F. Schutz, F. Seifert, A. M. Sintes, J. R. Smith, P. H. Sneddon, I. Taylor, R. Taylor, A. Thuering, C. Ungarelli, A. Vecchio, J. Veitch, H. Ward, U. Weiland, H. Welling, P. Williams, B. Willke, W. Winkler, G. Woan, and I. Zawischa, "The status of GEO 600," **Classical and Quantum Gravity**, vol. 22, no. 10, pp. S193————————S198, 2004.

[18] P. Bernard, G. Gemme, R. Parodi, and E. Picasso, "A detector of small harmonic displacements based on two coupled microwave cavities," **Review of Scientific Instruments**, vol. 72, no. 5, pp. 2428–2437, 2001.

[19] A. H. Guth, "Inflationary universe: A possible solution to the horizon and flatness problems," **Physical Review D**, vol. 23, no. 2, pp. 347–356, 1981.

[20] A. D. Linde, "Coleman-Weinberg theory and the new inflationary universe scenario," **Physics Letters B**, vol. 114, no. 6, pp. 431–435, 1982.

[21] A. Albrecht and P. J. Steinhardt, "Cosmology for grand unified theories with radiatively induced symmetry breaking," **Physical Review Letters**, vol. 48, no. 17, pp. 1220–1223, 1982.

[22] N. Barnaby, E. Pajer, and M. Peloso, "Gauge field production in axion inflation: Consequences for monodromy, non-Gaussianity in the CMB, and gravitational waves at interferometers," **Physical Review D - Particles, Fields, Gravitation and Cosmology**, vol. 85, no. 2, pp. 1–24, 2012.

[23] M. S. Turner, "Detectability of inflation-produced gravitational waves," **Physical Review D**, vol. 55, no. 2, pp. R435–R439, 1997.

[24] B. J. . Carr and S. Hawking, "Black Holes in the Early Universe," **Monthly Notices of the Royal Astronomical Society**, no. 168, pp. 399–, 1974.

[25] B. J. Carr, "The primordial black hole mass spectrum," **The Astrophysical Journal**, vol. 201, p. 1, oct 1975.

[26] B. J. Carr, K. Kohri, Y. Sendouda, and J. Yokoyama, "New cosmological constraints on primordial black holes," **Physical Review D**, vol. 81, p. 104019, may 2010.

[27] X. Siemens, V. Mandic, and J. Creighton, "Gravitational-wave stochastic background from cosmic strings," **Physical Review Letters**, vol. 98, no. 11, pp. 1–4, 2007.

[28] T. W. B. Kibble, "Topology of cosmic domains and strings," **Journal of Physics A: Mathematical and General**, vol. 9, no. 8, pp. 1387–1398, 1976.

[29] A. Vilenkin, "Cosmic strings and domain walls," **Physics Reports**, vol. 121, no. 5, pp. 263–315, 1985.

[30] C. J. Hogan, "Gravitational waves from light cosmic strings : Backgrounds and bursts with large loops," **Physical Review D**, vol. 74, no. August, pp. 1–10, 2006.

[31] A. Kosowsky and M. S. Turner, "Gravitational Waves from First-Order Cosmological Phase Transitions," **Physical Review Letters**, vol. 69, no. 14, pp. 2026–2029, 1992.

[32] The LIGO Scientific Collaboration, "Upper limits on a stochastic background of gravitational waves," **Physical Review Letters**, vol. 95, no. 22, pp. 1–6, 2005.

[33] R. H. Cyburt, B. D. Fields, K. A. Olive, and E. Skillman, "New BBN limits on physics beyond the standard model from 4He," **Astroparticle Physics**, vol. 23, no. 3, pp. 313–323, 2005.

[34] A. Kaiser, Nick ; Stebbins, "Microwave Anisotropy due to cosmic strings," **Nature**, vol. 310, pp. 391–393, 1984.

[35] I. Sendra and T. L. Smith, "Improved limits on short-wavelength gravitational waves from the cosmic microwave background," **Physical Review D - Particles, Fields, Gravitation and Cosmology**, vol. 85, no. 12, pp. 1–6, 2012.

[36] The LIGO Scientific Collaboration, "Searching for stochastic gravitational waves using data from the two colocated LIGO Hanford detectors," **PHYSICAL REVIEW D**, vol. 91, no. 222, pp. 22003–1550, 2015.

[37] The LIGO Scientific Collaboration, "An upper limit on the stochastic

gravitational-wave background of cosmological origin," **Nature**, vol. 460, no. 7258, pp. 990–994, 2009.

[38] The LIGO Scientific Collaboration, "Improved Upper Limits on the Stochastic Gravitational-Wave Background from 20092010 LIGO and Virgo Data," **Physical Review Letters**, vol. 113, p. 231101, dec 2014.

[39] B. J. Carr, "Primordial Black Holes and Quantum Effects," **arXiv preprint arXiv:1402.1437**, vol. 7, pp. 1–8, 2014.

[40] R. W. P. Drever, J. L. Hall, F. V. Kowalski, J. Hough, G. M. Ford, A. J. Munley, and H. Ward, "Laser phase and frequency stabilization using an optical resonator," **Applied Physics B**, vol. 31, no. 2, pp. 97–105, 1983.

[41] R. Lanza, **Experimental Limits of Gravitational Waves in the MHz Frequency Range**. PhD thesis, University of Chicago, 2015.

[42] L. McCuller, **Testing a model of Planck-Scale Quantum Geomtery with Broadband Correlation of CoLocated 40M Interferometers**. PhD thesis, University of Chicago, 2015.

[43] E. D. Black, "An introduction to PoundDreverHall laser frequency stabilization," **American Journal of Physics**, vol. 69, p. 79, jan 2001.

[44] S. L. Larson, W. Hiscock, and R. Hellings, "Sensitivity curves for spaceborne gravitational wave interferometers," **Physical Review D**, vol. 62, no. 6, p. 062001, 2000.

[45] R. Weiss, "Electromagnetically Coupled Broadband Gravitational Antenna," **Quarterly report of the Research Laboratory for Electronics, MIT**, 1972.

[46] S. L. Larson, "Gravitational Waves."

[47] B. F. Schutz, "Networks of gravitational wave detectors and three figures of merit," **Classical and Quantum Gravity**, vol. 28, no. 12, p. 125023, 2011.

[48] P. Peters and J. Mathews, "Peters_Mathews_PR_131_435_1963.pdf," **Physical Review**, vol. 131, no. 1, 1963.